UPPSALA
UNIVERSITET

Digital Comprehensive Summaries of Uppsala Dissertations from the Faculty of Science and Technology 420

Synchrotron Radiation Studies of Free and Adsorbed Molecules

ZHUO BAO

ACTA
UNIVERSITATIS
UPSALIENSIS
UPPSALA
2008

ISSN 1651-6214
ISBN 978-91-554-7150-7
urn:nbn:se:uu:diva-8610

Dissertation presented at Uppsala University to be publicly examined in Polhemsalen, Ångströmlaboratoriet, Lägerhyddsvägen 1, Uppsala, Friday, April 25, 2008 at 13:15 for the degree of Doctor of Philosophy. The examination will be conducted in English.

Abstract
Bao, Z. 2008. Synchrotron Radiation Studies of Free and Adsorbed Molecules. Acta Universitatis Upsaliensis. *Digital Comprehensive Summaries of Uppsala Dissertations from the Faculty of Science and Technology* 420. xiv, 55 pp. Uppsala. ISBN 978-91-554-7150-7.

This thesis contains two parts. The first part concerns the research work on free molecules using synchrotron-radiation-related techniques. Auger electron spectra of two free open-shell molecules, O_2 and NO, were studied experimentally and theoretically. Photoionization experimental technique with tunable synchrotron radiation source was used to induce core-level electron ionization and obtain the *KVV* normal Auger electron spectra. A quantitative assignment of O_2 normal Auger spectrum was obtained by applying *ab initio* CI calculations and LVI Auger line shape simulations including the bond length dependence of Auger transition rates. The photon energy dependence of normal Auger electron spectra was focused on with photon energies in the vicinities of core-ionization threshold energies. Consequently, the MAPCI (Molecular Auger Post Collision Interaction) theory was developed. Taking the near-threshold O_2 normal Auger spectrum as an example, the two extreme cases of MAPCI effect, "atomic-like PCI" and "molecular PCI", were discovered and discussed. The effect of shape resonance on near-threshold molecular normal Auger spectrum was discussed taking NO near threshold normal Auger spectra as example.

The second part deals with research work on the chemisorption of small epoxy organic molecules, ethylene oxide, methyl oxirane, on Si (100) surfaces. Synchrotron radiation related techniques, UPS, XPS and NEXAFS, were applied. Based on the valence photoemission spectra, C 1*s* and Si 2*p* XPS spectra, the epoxy ring opening reactions of these molecules in chemisorption process were proved. Further tentative search for the surface-adsorbate CDAD effect was performed, and no evident circular dichroism was confirmed.

Keywords: Synchrotron radiation, Auger electron spectroscopy, one-step model, Post Collision Interaction (PCI), theoretical modeling, molecules, adsorbates, UPS, XPS, XAS, NEXAFS

Zhuo Bao, Department of Physics and Materials Science, Surface and Interface Science Division, Ångströmlaboratoriet, Lägerhyddsv. 1, Box 530, Uppsala University, SE-75121 Uppsala, Sweden

ISSN 1651-6214
ISBN 978-91-554-7150-7
urn:nbn:se:uu:diva-8610 (http://urn.kb.se/resolve?urn=urn:nbn:se:uu:diva-8610)

To my wife, Lunmei Huang

List of Papers

This thesis is based on the following papers, which are referred to in the text by their Roman numerals.

Main bibliography for this thesis

I **Detailed Theoretical and Experimental Description of Normal Auger Decay in O_2**
Z. Bao, R. F. Fink, O. Travnikova, D. Céolin, S. Svensson and M. N. Piancastelli
Submitted to J. Phys. B

II **The PCI Effect in the O_2 Near Threshold Molecular Normal Auger Spectra**
Z. Bao, R. F. Fink, O. Travnikova, D. Céolin, I. Hjelte, A. Kivimäki and M. N. Piancastelli
In manuscript

III **Shape Resonance Affected Molecular Auger Post Collision Interaction (MAPCI) Effect of NO N K-edge Near Threshold Normal Auger Spectra**
Z. Bao, O. Travnikova, D. Céolin, R. F. Fink, and M. N. Piancastelli
In manuscript

IV **Electronic Structure of Core-excited and Core-ionized Methyl Oxirane**
M. N. Piancastelli, T. Lischke, G. Prümper, X. J. Liu, H. Fukuzawa, M. Hoshino, T. Tanaka, H. Tanaka, J. Harries, Y. Tamenori, Z. Bao, O. Travnikova, D. Céolin and K. Ueda
Journal of Electron Spectroscopy and Related Phenomena vol.156-158, (2007) p.259-264

V **Electronic and Geometric Structure of Methyl Oxirane Adsorbed on Si (100)** 2×1
M. N. Piancastelli, Z. Bao, F. Hennies, O. Travnikova, D. Céolin, T. Kampen and K. Horn
Applied Surface Science, vol.254, (2007) p.108-112

VI **The Bonding of Chemisorbed Ethylene Oxide on Si (100) Surface**
F. Hennies, Z. Bao, O. Travnikova and M. N. Piancastelli
In manuscript

VII **Search for Circular Dichroism Effects in Methyl Oxirane Adsorbed on Si (100)**
M. N. Piancastelli, Z. Bao, O. Travnikova, T. Kampen, P. Schmidt, T. Deniozou, T. Braun and K. Horn
Submitted to Surf. Sci.

Reprints were made with permission from the publishers.

The following is a list of publications to which I have contributed to. They will not be included in this thesis.
Extended bibliography

1. **Chemisorption of Methyl Oxirane on Si(100)** 2×1 **Surface: Studied by NEXAFS and TD-DFT method**
Z. Bao, O. Travnikova, F. Hennies and M. N. Piancastelli
In manuscript

2. **Photoemission, NEXAFS and TD-DFT Method Study Chemisorption of Small Epoxy Molecules on Si(100)** 2×1 **surface: Ethylene oxide, Methyl Oxirane, cis-Dimethyl oxirane, trans-Dimethyl oxirane**
Z. Bao, O. Travnikova, F. Hennies and M. N. Piancastelli
In manuscript

3. **Study of the Dissociation of Nitrous Oxide Following Resonant Excitation of the Nitrogen and Oxygen K-shells**
D. Céolin, O. Travnikova, Z. Bao, M. N. Piancastelli, T. Tanaka, M. Hoshino, H. Kato, H. Tanaka, J. R. Harries, Y. Tamenori, C. Prümper, T. Lischke, X. -J. Liu and K. Ueda
J. Chem. Phys. vol.128, (2008) 024306

4. **A High-resolution Study of Resonant Auger Decay Processes in N_2O After Core Electron Excitation from Terminal Nitrogen, Central Nitrogen and Oxygen Atoms to the 3π LUMO**
M. N. Piancastelli, D. Céolin, O. Travnikova, Z. Bao, M. Hoshino, T. Tanaka, H. Kato, H. Tanaka, J. R. Harries, Y. Tamenori, G. Prümper, T. Lischke, X.-J. Liu and K. Ueda
J. Phys. B: At. Mol. Opt. Phys. vol.40, (2007) p.3357-3365

5. **Disentangling the Complex Line Profiles in the Cl $2p$ Photoelectron Spectra of Cl_2**
   O. Travnikova, R. F. Fink, A. Kivimäki, D. Céolin, Z. Bao and M. N. Piancastelli
   Chemical Physics Letters vol.426, (2006) p.452-458

6. **Phase and Molecular Orientation in Metal-free Phthalocyanine Films on Conducting Glass: Characterization of Two Deposition Methods**
   Y. Alfredsson, J. Åhlund, K. Nilson, L. Kjeldgaard, J. N. O'Shea, J. Theobald, Z. Bao, N. Mårtensson, A. Sandell, C. Puglia and H. Siegbahn
   Thin Solid Films vol.493, (2005) p.13-19

7. **A Study of Substituent Effects for Aliphatic CH_3-X Compounds by Resonant Auger Spectroscopy.**
   O. Travnikova, S. Svensson, D. Céolin, Z. Bao, and M. N. Piancastelli
   In manuscript

8. **New Assignment of $L_{2,3}MM$ Normal Auger Decay Spectrum of Cl_2 by *ab initio* Calculations**
   O. Travnikova, R. F. Fink, D. Céolin, Z. Bao and M. N. Piancastelli
   In manuscript

9. **A Detailed Study of Electron Decay Processes Following $2p$ Core Excitation in Cl_2**
   M. N. Piancastelli, O. Travnikova, Z. Bao, D. Céolin and A. Kivimäki
   In manuscript

Comments on My Own Participation

All the papers included in this thesis are the results of team work and cooperations, and my contributions for them are different.

In the work of Paper **I**, I made the detailed calculation plan and performed all the programming, calculations, Auger line shape simulations, curve-fitting and assignment. I was also responsible for the redaction of manuscript.

In Paper **II** and Paper **III**, I was the team member in the experiments and data acquisitions. I developed and formulated the MAPCI theory, made the programming and spectrum simulations. I was responsible for the manuscripts.

In Paper **IV**, I took part in the experiments and data acquisition work.

In Paper **V**, Paper **VI** and Paper **VII**, I was responsible for the plannings and runnings of the experiments and data acquisitions. I made the data treatments and joined the data analysis and manuscript writings.

List of Abbreviations

A

AES	Auger Electron Spectroscopy
ARPES	Angular Resolved PhotoEmission Spectroscopy

C

CCD	Charge-Coupled Device
CD	Circular Dichroism
CDAD	Circular Dichroism in Angular Distribution

D

DFT	Density Functional Theory
DVR	Discrete Variable Representation

F

FWHM	Full Width at Half Maximum

H

HAD	High Angular Dispersion

L

LAD	Low Angular Dispersion
LDOS	Local Density of States
LEED	Low Energy Electron Diffraction
LVI	Lifetime Vibrational Interference

M

MAD	Medium Angular Dispersion
MAPCI	Molecular Auger Post Collision Interaction
MCP	MicroChannel Plate detector
MPCIR	Molecular Post Collision Interaction Resonance

N

NEXAFS	Near Edge X-ray Absorption Fine Structure

P

PCI	Post Collision Interaction
PEPICO	Photo-Electron Photo-Ion COincidence

R

RAS	Resonant Auger electron Spectroscopy
RDLVI	(bond length) R-Dependent Lifetime Vibrational Interference

T

TD-DFT	Time Dependent Density Functional Theory
TIY	Total Ion Yield

U

UPS	Ultraviolet Photoelectron Spectroscopy

W

WAD	Wide Angular Dispersion

X

XAS	X-ray Absorption Spectroscopy
XES	X-ray Emission Spectroscopy
XPS	X-ray Photoelectron Spectroscopy
XVUV	Extreme Vacuum UltraViolet

Contents

Part I:
Conceptual Introduction

1. Populärvetenskaplig Sammanfattning

1.1 Elektronhöljets Fysik, Studier av Fria och Adsorberade Molekyler

Under de senare decennierna har elektronhöljets fysik vuxit som forskningsområde. Det finns många orsaker till detta; en viktig drivkraft har emellertid varit att helt nya så kallade icke-konventionella ljuskällor tillkommit. Lasern är ju ett välkänt verktyg i detta sammanhang. Vid sidan av lasern har emellertid har en ny källa för elektromagnetisk strålning utvecklats: Synkrotronljuset.

1.2 Vad är Synkrotronljus?

Elektromagnetisk strålning uppstår då elektriska laddningar accelereras. Synkrotronljuset utsänds av elektriska laddningar, i praktiken antingen elektroner eller positroner, som i en accelerator har fått *relativistiska energier*. När sådana laddningar accelereras, dvs när de avböjs i magnetiska fält, utsänds synkrotronstrålning. Termen synkrotronstrålning är något oegentlig eftersom de flesta synkrotronljusanläggningar utnyttjar en s.k. *lagringsring* som inte är en accelerator utan en ring där elektroner lagras vid hög (relativistisk) energi. Vid den svenska anlägganingen MAX laboratoriet finns f.n. tre lagringsringar för produktion av synkrotronljus i drift. En fjärde är planerad (MAX IV) och kommer när den byggts att bli världens främsta synkrotronljusring.

1.3 Innerskalselektroner

Elektronerna i atomer och molekyler har bestämda energinivåer. Man talar o matt de befinner sig i olika skal. Denna nomenklatur ger en bra uppfattning av elektronfördelningen eftersom elektronerna faktiskt fördelar sig kring atomkärnan i en struktur som liknar skal i en kinesisk ask. Den allra viktigaste distinktionen vad gäller skalen är den mellan *ytterskalselektroner* och *innerskalselektroner*. Det är bara elektronerna i det yttersta skalet i en viss atom i en molekyl som kan växelverka *direkt* med elektronerna i de andra atomerna i samma molekyl. Innerelektronerna befinner sig i närheten av atomkärnan och är alltså mycket atomär till sin karaktär

Innerskalselektronerna i ett en molekyl är specifika för atomslaget, de känner av de lokala egenskaperna t.ex.för en molekyl, eller en molekyl på en metallyta (en sådan kallas adsorbat) , eller en atom i en halvledare. Detta gör att spektroskopi som utnyttjar vakanser i en innerelektronnivå (*Innerhålsspektroskopi*) är mycket användbar. En av de viktigaste framstegen som åstadkommits genom synkrotronljuset är att det möjliggjort nya typer av studer av *innerdskalselektroner* i atomer, molekyler vätskor och fasta material.

1.4 Elektronspektroskopi

Elektronspektroskopi är en av de mest använda teknikerna som utnyttjar synkrotronljus för att studera både gasformiga, vätskeformiga material samt ytor av fasta material. Den moderna högupplösande elektronspektroskopin utvecklades på femtiotalet av Kai Siegbahn (Nobelpris 1981) och hans studenter. Denna spektroskopi bygger på att man kan mäta kinetiska energin hos elektroner. Principen är mycket enkel och bygger på elektrostatisk deflektion av elektronerna. Det finns många varianter av moderna spektrometrar. Mest använd är elektrostatiska spektrometrar. De elektroner som skall energianalyseras släpps in mellan två laddade elektroder. Genom avlänkning i det elektrostatiska fältet kommer elektroner med olika kinetisk energi att lägessepareras vid detektionsplanet, där en s.k. multikanalplatta kan utnyttjas som detektor. Signalen från detektorn, som förstås måste undergå "massage" av en dator, ger information om hur många elektroner som kommer ut vid en viss kinetisk energi E_k.

1.5 Fotoelektronspektroskopi och Augerelektronspektroskopi

Pierre Auger upptäckte på tjugotalet att om ett prov belyses med röntgenstrålning så kommer det ut två slags elektroner. Fotoelektronerna, har vi talat om ovan, har en energi beror av röntgenstrålningens våglängd, dvs av fotonernas energi. Dessutom upptäckte Augerelektroner vars energi inte ändras med röntgenstrålningens energi. Dessa har fått namnet *Augerelektroner*.

Den kinetiska energin som fotoelektronerna erhåller ges av Einsteins berömda fotoelektriska lag:

$$E_k = h\nu - E_{\,(Innerelektron\,joniserade\ \ tillståndet)} - E_{\,(Grundtillståndet)}$$

Där $h\nu$ är den absorberade fotonens energi.

Augerelektronerna har vi redan behandlat ovan. Eftersom Augerprocessen innebär att den energi som jonen erhållit via fotojonisation deexciteras och överlämnas till elektronen kommer Augerelektronens energi att kunna skrivas

som:

$$E_k = E_{\,(Innerelektron\,joniserade\ \ tillståndet)} - E_{\,(Dubbel\,joniserade\ \ tillståndet)}$$

Detta innebär att Augerelektronernas energi är oberoende av energin hos de fotoner som skapade innerelektronvakansen. Om fotonenergin ändras ligger Augerelektronernas kinetiska energi still. Detta är ett mycket effektivt sätt att experimentellt klarlägga skillnaden mellan det två typerna av elektroner. Med synkrotronljus kan man enkelt ändra fotonenergin och därmed se vilka elektroner som kommer ut med konstant energi och vilka som ändrar energi och således är fotoelektroner.

I avhandlingen redovisas resultat rörande elektronhöljet såväl fria molekyler som molekyler på ytor. De experimentella resultaten har behandlats med teoretiska modeller och visar hur man med synkrotronljus och elektronspektroskopi kan erhålla en mycket detaljerad kunskap om de molekylära systemen.

2. Introduction

In chaos Nature's laws hid veiled in night. God said, "Let Crystal be," and all was light. It did not last; the devil howling "Ho! Let Surface be!" restored the status quo.
-anonymous, after Alexander Pope

A good reason to carry out fundamental research on isolated molecules is that in the universe more than 99.99% of visible matter is in gas-phase. Understanding what happens for gas-phase matter means understanding the basic rules of the cosmos. So it is necessary for us to experimentally and theoretically study free molecules before starting our "star trek". In outer space, for example, the road from the Solar System to the Pleiades Star Cluster is full of radiation in the energy range of soft and hard X-rays. This radiation is produced by high-energy reactions of stars and travels in a distance of millions of light years in the ultra high vacuum environment. The important interactions between these high energy photons and matters are core-level electron ionizations and excitations in atoms and molecules. These processes are mostly interesting subjects of current scientific research.

As a powerful tool, synchrotron radiation has been used in many scientific areas like gas-phase molecules, surface and interface studies, material science and biology. At synchrotron radiation facilities, we can obtain monochromatized and tunable X-ray radiation. During my Ph. D. period, our research group has focused on using this tool to explore the principles of molecular core-level electronic and nuclear dynamics and semiconductor surface chemistry processes.

Figure 2.1: The Pleiades Star Cluster.

Beside the use of experimental methods, to understand the intrinsic complexity of these processes, we have also shared our efforts on learning, developing and applying novel theoretical methods.

This thesis is a summary of part of my research works in the last few years. The instrumentation that we used on synchrotron radiation facilities is described in Chapter 3. The basic experimental methods and theoretical methods

are described in Chapter 4. The results of the papers included are discussed and summarized in Chapter 5. All the papers are included in Part II.

This thesis is based on seven papers, belonging to two main subjects. Paper **I**, **II**, **III** and **IV** concentrate on the experimental and theoretical studies of free molecule core-hole relaxation dynamics. Papers **V** ,**VI** and **VII** contain the studies of small epoxy organic molecules chemisorbed on the Si (100) surface.

3. Instrumentation

3.1 Synchrotron Radiation

Synchrotron radiation is one of the most flexible light sources in terms of wavelength tunability available nowadays. In this chapter, its general properties and some examples of instrumentation we have used will be briefly described.

3.1.1 What is Synchrotron Radiation ?

The synchrotron radiation is named after a kind of particle accelerator called "synchrotron". In a synchrotron, charged particles, typically the electrons, are accelerated around a fixed circular path by an electric field. At the same time of kinetic energy increasing of charged particles, the magnetic field in synchrotron will also be increased to hold the particle path. The accelerated charged particles can produce a photon beam with a wide wavelength range. It is called "synchrotron radiation".

As a natural result of adding an acceleration perpendicular to the velocity of the charges, the radiation emitted from the charge is characteristic of the particle speed and trajectory. Since one of the properties of synchrotron radiation is the very extended energy range, from far infrared to hard X-rays, its usage bloomed quickly since its discovery in the year 1946. At the beginning, synchrotron radiation was only generated as a byproduct of particle accelerators, and these devices are called first-generation sources. The second-generation sources are storage rings dedicated to synchrotron radiation and equipped with bending magnets. The third-generation facilities are characterized by insertion devices, namely undulators and wigglers, which produce more intense and better-quality radiation.

3.1.2 Bending Magnet

A bending magnet is one of the simplest instrumentations that can produce synchrotron radiation. In the magnetic field, the electron with kinetic energy around 1 GeV and velocity near to light speed feels an acceleration perpendicular to its trajectory and emits photons. Because of the speed of the electron, most of the photons are emitted in a small forward solid angle, which is called the "central radiation cone". As shown in figure 3.1, the radiation spectrum of bending magnets radiation is like the black-body radiation, a continuum spectrum. The radiation photon energy with highest radiation intensity is expressed

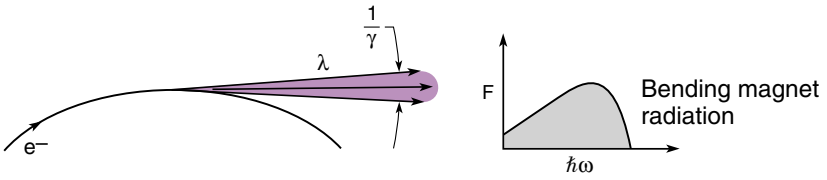

Figure 3.1: Electron trajectory in bending magnet and synchrotron radiation energy distribution, "F" is the flux and "$\hbar\omega$" is the photon energy. [1].

in Eq. 3.1. It is related to the electron velocity v and the magnetic field B.

$$E_c = \frac{3e\hbar B\gamma^2}{2m} \tag{3.1}$$

$$\gamma = 1\Big/\sqrt{1-\frac{v^2}{c^2}} \tag{3.2}$$

$$E_c(keV) = 0.6650E_e^2\ (GeV)\ B\ (T) \tag{3.3}$$

At the second-generation synchrotron radiation facilities, the electron beam positions, currents and electron kinetic energies are all optimized for better brilliance [1], photon flux, spot size and beam stability. To achieve better beam performance, the "insertion devices" were developed and used.

3.1.3 Insertion Devices

The third-generation synchrotron radiation facility is characterized by the application of "insertion devices". There are two kinds of insertion devices: undulator and wiggler. Both of them are composed by periodical magnets, as shown in Figure 3.2. They have similar structures but different magnitude of the magnetic field. The electrons with GeV kinetic energy move along the insertion devices, and the periodical magnetic field makes the trajectory of electron undulating or wiggling.

$$\lambda = \frac{\lambda_u}{2\gamma^2}\left(1+\frac{K^2}{2}+\gamma^2\theta^2\right) \tag{3.4}$$

$$K = \frac{eB_0\lambda_u}{2\pi mc} = 0.9337B_0\,(T)\,\lambda_u\,(cm) \tag{3.5}$$

$$E(keV) = \frac{0.9496E_e^2\ (GeV)}{\lambda_u\,(cm)\left(1+\frac{K^2}{2}+\gamma^2\theta^2\right)} \tag{3.6}$$

[1] Brilliance = $Photons/(Time \times S\,pot\,Size \times Convergence \times 0.1\%Band\ Width)$

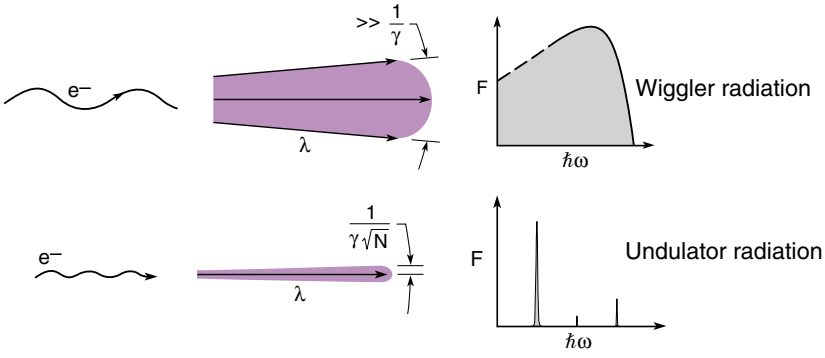

Figure 3.3: Comparison of undulator and wiggler for the electron trajectories and their radiation energy distributions [1]. "F" is the radiation flux.

An undulator is characterized by relatively weaker periodical magnetic field than the wiggler and, as shown in Figure 3.3, its radiation is characterized by line spectrum, partial coherence and small emittance. The electron trajectory in an undulator has small amplitude diverging from the central position due to weak magnetic field intensity, meaning that $K \ll 1$ in Eq. 3.4, and the effective speed of electron (projected velocity on the moving direction of electron) is almost equals to the light speed. Eq. 3.4 shows that the photon energy of the harmonics generated by the undulator depends upon the intensity of magnetic field which can be finely tuned by changing the gap of the undulator, the magnet period length and the electron beam energy.

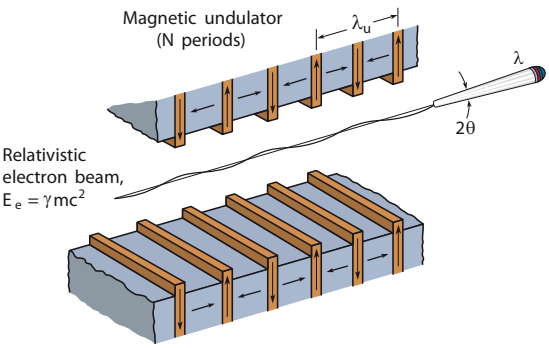

Figure 3.2: The structure of an undulator [1].

The radiation polarization is related to the trajectory of electrons in the insertion devices. In the most common case, with the homogeneous magnetic field in the gap of the undulator, the electron undulates in the plan perpendicular to the magnetic field. Hence linear polarized radiation is obtained with the photon electric-field-vector perpendicular to the undulator magnetic field. Some advanced undulators have modified magnetic field patterns, and they can provide more flexible choices, like elliptically and circularly polarized lights and possibilities of changing both the polarization and the electric-field-vector

direction of the radiation in experiments. Typical examples are the undulators available in synchrotron facilities BESSY (Germany) and SPring-8 (Japan).

A wiggler is another kind of insertion device. It has much stronger periodical magnetic field comparing to an undulator. The K value in Eq. 3.4 is much larger than 1 in the case of wiggler. The effective speed of electrons in a wiggler is much smaller than the light speed and destroys the coherence of the radiation. So the wiggler radiation has a dipole-like spectrum distribution and is often used to obtain higher intensity for hard X-ray radiations used for crystallography-related techniques.

All our experiments were performed on undulator beamlines.

3.2 Hemispherical Electron Analyzer

In the interaction between synchrotron radiation and atoms, molecules and surfaces, with enough photon energy, emitted electrons can be detected. These electrons may not only be produced by photoionization process, but could also be produced in the Auger decay process or autoionization process. By detecting the binding energy, energy distribution (line shape and line width) and photon energy dependence and electron emission angular distribution, enormous information can be obtained for the electronic structure, electronic and nuclear dynamics, atomic bonding characters, macro-structures and so on. To detect the electron, different kinds of electron energy analyzers are widely used in various scientific areas. Hemispherical electron energy analyzers are one the most popular type of analyzers used together with synchrotron radiation for medium and high kinetic energy electrons (>10 eV). In this thesis, two types of commercial hemispherical electron analyzers are used, one is the Scienta R4000 electron analyzer from VG Scienta company, and the other one is the PHOIBOS 100 electron analyzer from SPECS GmbH. We have used them to measure the electron kinetic energy, electron yield and electron emission angular distribution in different projects.

3.2.1 General Principles

As shown in Figure 3.4, a typical hemispherical electron analyzer is composed by several parts. The first part (1 in Figure 3.4) is composed by electrodes putting bias voltages on electrons emitted from sample. By optimizing the bias voltages, the low electron collection rate due to the deviations of sample position from the focus position of analyzer can be greatly improved. In Scienta R4000, these electron collecting electrodes are called “up”, “down”, “left” and “right”. The second part (2 in Figure 3.4) of the analyzer are the retarding/accelerating electrodes. In this part the retarding/accelerating voltage adjusts the electron kinetic energy to the value of the chosen pass energy E_p, and by scanning this voltage, the scanning of electron kinetic energy can

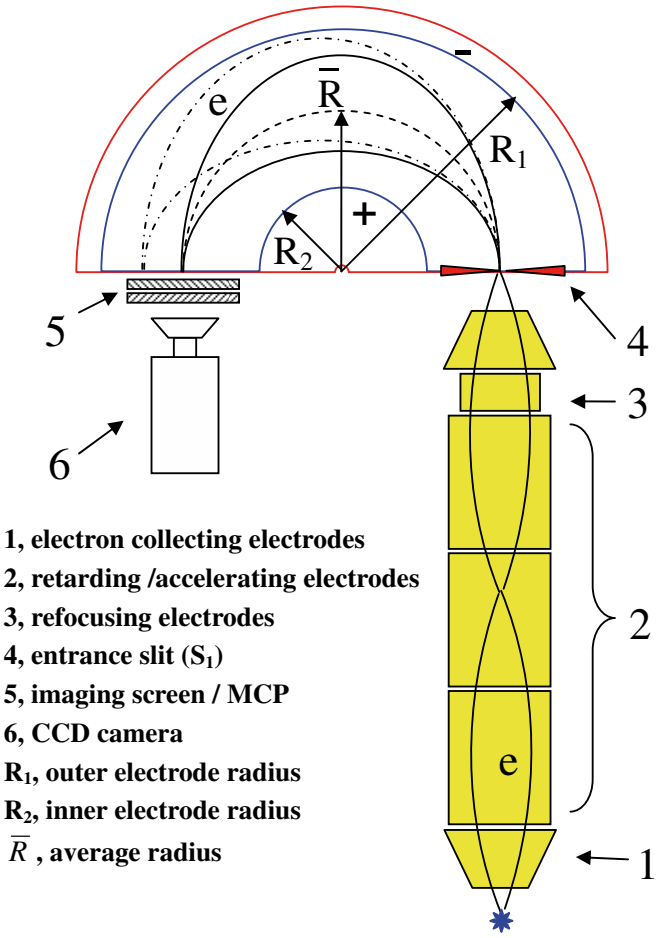

Figure 3.4: The principle structure of hemispherical electron energy analyzer. Qualitatively, the electron trajectories in the hemispherical part correspond to different enter angles and kinetic energies. The solid lines correspond to the trajectories of electrons with kinetic energy of E_p, dot lines (- · -) correspond to the trajectories of electrons with higher kinetic energies.

be performed. After this part, the electrons with kinetic energies close to E_p will be refocused by electrodes (3) and go through the entrance slit, which has a slit size of S_1, into the hemispherical part. The hemispherical part is composed by a outer electrode with radius of R_1 and a inner electrode with radius of R_2. $\bar{R} = (R_1 + R_2)/2$ is the mean radius. By applying voltages between the outer and inner hemispheres, the electrons with different kinetic energies can be dispersed. As shown in Figure 3.4, in the hemispherical part, the electron having kinetic energy of pass energy (E_p (eV), corresponding to the hemisphere voltage (V)) will be imaged in the middle of the detector located at the

end of hemisphere. Those with higher or lower kinetic energies will hit the position on detector off the center. The imaged electrons will be displayed by the MCP/screen at the end of hemisphere. The energy and angular dispersions of these electron signals will be detected by a 2D CCD camera and digitally transferred to the computer.

In measurements, as expressed by Eq. 3.7, the energy resolution ΔE is related to the pass energy E_p, the entrance slit size S_1 and the analyzer constant mean radius $\bar{R}$. So, in actual application to obtain a fixed instrumental energy resolution for electrons with various kinetic energies, the pass energy E_p and entrance slit size S_1 are usually fixed when the electron kinetic energy is being scanned.

$$\Delta E = E_p \times \frac{S_1}{2 \cdot \bar{R}}. \tag{3.7}$$

3.2.2 Angular Resolved Photoemission

As mentioned at the beginning of this section, besides the binding energy and line shape, the electron emission angular distribution does also contain plenty of important information. The angular resolved photoemission spectroscopy (ARPES) technique is one of the hottest techniques applied in surface science and studies of low dimension systems [2]. From the angular distribution, surface and bulk band structures, surface morphology, molecular structure and chiral properties can be derived. In our works, we have attempted to search for the circular dichroism of methyl oxirane adsorbed Si(100) surface using the ARPES technique with PHOIBOS 100 electron analyzer, in Paper **VII**. The electron optical systems of a hemispherical electron energy analyzer can be optimized for different purposes, e.g. real space imaging, inverse space imaging (angular imaging) or improving electron transmissions [3]. For the purpose of obtaining the emission angle information, SPECS PHOIBOS 100 electron analyzer provides several angular dispersion control modes. HAD (High Angular Dispersion) mode can image the emission angle of ±3°, MAD (Medium Angular Dispersion) mode can image the emission angle of ±4°, LAD (Low Angular Dispersion) mode images the emission angle of ±7° and WAD (Wide Angle Dispersion) mode images the emission angle of ±13°. As shown in Fig. 3.5, in these modes the electron emission angles are imaged rather than the real space. With the help of 2D CCD camera, both the emission angle distribution and kinetic energy distribution can be obtained simultaneously.

3.3 Beamlines and Experimental Setups

A “beamline” includes the source of synchrotron radiation, namely either a bending magnet or an insertion device, the optical system and the “end station”. The radiation source determines the basic character of the radiation, like photon energy range, brilliance, photon polarization. The optical system

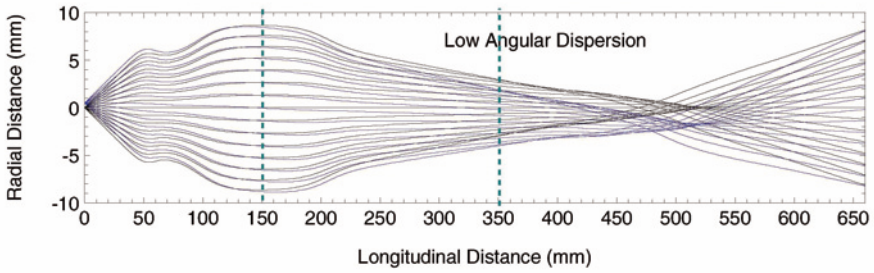

Figure 3.5: The simulated electron trajectories in the PHOIBOS 100 electron analyzer under the angular dispersion mode of LAD (Low Angular Dispersion) [3]. The trajectories in blue and black are from separated spatial points on sample. In the "Longitudinal Distance", the sample is placed at 0 mm, the iris is located at 150 mm, the hemispherical part starts from 350 mm, ends at 660 mm where the electron emission angular distribution is imaged. The view point in this figure is from the side of Figure 3.4.

usually consists of several slits, focusing mirrors and, most important, a monochromator. By the optical system, the photons, usually in the energy range of 50 eV to 1500 eV, are monochromatized and transferred to the experimental chamber at the end station, which is equipped with various instruments for data acquisition.

3.3.1 MAX II, I411 and I511

MAX-lab is the national laboratory of Sweden which is dedicated to accelerator physics, nuclear physics and synchrotron radiation-based research. Our experimental work was performed on beamlines I411 and I511, which are installed on the 1.5 GeV electron energy, third-generation electron storage ring MAX II.

Beamline I411 is mainly dedicated to gas-phase research with soft X-rays. The undulator installed has 44.5 periods and λ_u=58.8 mm period length. It produces soft X-ray photons in the energy range from 50 eV to 1500 eV [4]. The monochromator installed is a Zeiss SX700 with plane grating [5]. The experimental end station is equipped with a commercial hemispherical electron energy analyzer Scienta R4000. The electron energy analyzer can be either rotated around the photon beam direction to perform angle-resolved measurement, or it can be placed at the "magic angle", 54.7° relative to the electric-field-vector of radiation, to avoid angular distribution effects. To obtain good signal intensity, a gas cell is usually used in our experiment to increase the pressure of the sample without breaking the vacuum of the whole system and affecting the free path length of free electrons. The working pressure we used

is around 10^{-6} Torr in the main chamber. On this beamline, experiments can be performed using UPS, XPS, XAS, AES, coincidence and other techniques.

Our surface experiments were performed on beamline I511 [6], which has two branches, one for surface-related experiments and the other one for bulk-related experiments. This beamline is using the same type of undulator and monochromator as beamline I411. With a flip mirror, the radiation beam can be transferred to either one of the end stations. Before the end station of surface branch, two elliptical mirrors focus the radiation beam at the measuring position. The end station has two experimental chambers, the analysis chamber and the preparation chamber. On the preparation chamber, LEED, mass spectrometer and ion sputter gun are installed for clean surface and adsorbed surface preparation and characterization. A 3-dimensional motor-controlled manipulator is to hold the sample and transfer the sample between the two chambers. On the analysis chamber, a SES-R4000 commercial hemispheric electron energy analyzer and a XES spectrometer are installed. They can be rotated around the beam axis and high resolution angular-resolved UPS, XPS, XAS, AES and XES spectra can be obtained.

3.3.2 BESSY, UE56-2

BESSY, "Berliner Elektronenspeicherring-Gesellschaft für Synchrotronstrahlung", Berlin, Germany, has a 1.7 GeV storage ring. We used the UE56-2-PGM1 surface science beamline, which is equipped with specially designed undulators allowing fast switching of synchrotron radiation polarization [7, 8]. The beamline has two Sasaki-type elliptically polarizing undulator modules as light source. As shown in Figure 3.6, the undulator has four groups of periodical magnets. By changing the relative positions of them, the vertically and horizontally linear polarized light, positively and negatively circular polarized light and other elliptically polarized light can be obtained.

With the plane grating monochromator, a beamline resolving power [2] of 6000 to 13000 can be obtained for photon energy from 89 to 1328 eV [8]. The end station is equipped with a SPECS PHOIBOS 100 electron analyzer with which experiment of XPS, NEXAFS, UPS can be performed. The sample is held by a "five and a half dimensions" (X, Y, Z, rotation around manipulator axis, rotation around surface vector, flipping up and down) manipulator. With the help of this manipulator, full angular resolved experiments can be performed by using the angular dispersion modes of the PHOIBOS 100. Thanks to the ability of fast switching synchrotron radiation polarizations, experiments for surface circular dichroism can be performed.

[2] *Resolving power* $= E_{photon}/\Delta E$

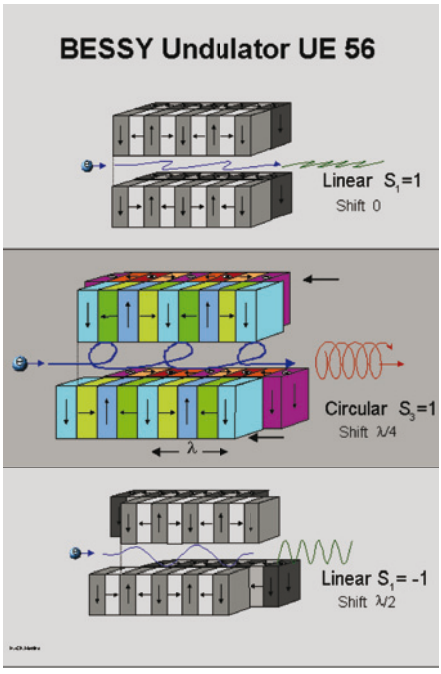

Figure 3.6: BESSY fast switching Sasaki type elliptically polarizing undulator [9].

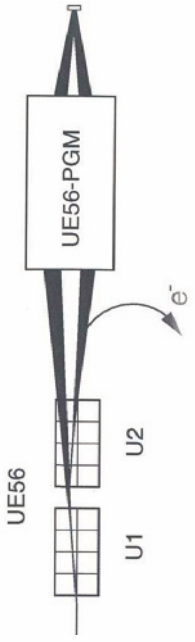

Figure 3.7: UE56 beamline optics pattern [10].

3.3.3 SPring-8, 27SU

SPring-8, Japan, is a high-performance synchrotron radiation facility with really high primary electron energy, 8 GeV. We used the *C* branch of the BL27SU beamline [11, 12], which is designed for gas-phase experiment. One particularity of this beamline is the use of "figure-8" undulator.

As shown in Figure 3.8 and 3.9, the electron in "figure-8" undulator travels in a way such that looking in the direction of the electron beam, the electron trajectory looks like a "**8**" shape. This undulator has the ability to fast switch the electric-field-vector direction of linear polarized light. The integer harmonics of the radiation have the electric-field-vector perpendicular to that of the half integer harmonics. A Hettrick type monochromator [11] is installed on this beamline and photon energies from 170 eV to 2800 eV are provided. The end stations are equipped with a high-resolution Scienta SES-2002 electron energy analyzer, time-of-flight mass spectrometers and one energy analyzed electron-ion coincidence

instrument. Experiments of XPS, XAS by Auger electron yield, symmetry resolved XAS by photo-ion yield and PEPICO can be performed.

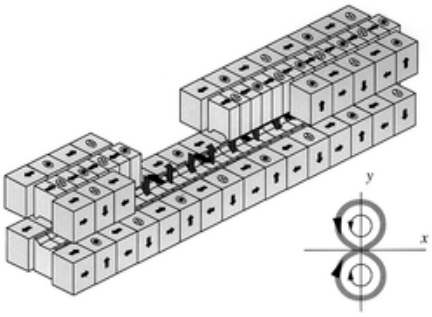

Figure 3.8: Magnetic structure of figure-8 undulator [13].

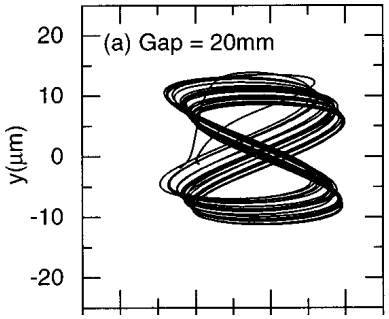

Figure 3.9: Electron trajectory in the figure-8 undulator seeing from the beam direction [14].

4. Experimental and Theoretical Methods

Our research line has been focused on the study of the electronic structures of free molecules and adsorbate systems. Based on the knowledge obtained, the complex electronic and nuclear dynamics, which is involved during or following the interactions between VUV, soft X-rays photons and the molecules and surfaces, were intensively studied. In studying the electronic structure and dynamics, the atomic and molecular orbital picture was used to describe the electron behaviors. The "core orbitals" have high binding energies, which are in the order of hundred eV. They are closely localized around the nuclei and behave atomically. The "valence orbitals" have low binding energies, which are in the order of ten eV. They are generally delocalized in case of a molecule. As the populated orbitals are called "occupied orbitals", some "unoccupied orbitals" also exist. To study the nature of these orbitals, UPS, XPS and XAS techniques (named as NEXAFS, TIY and symmetry-resolved photo-ion yield in different purposes and methods) were developed and widely applied in various scientific fields. Further information of core-hole electronic decay process and core-hole nuclear dynamics can be obtained by AES, RAS and XES techniques.

4.1 Vibrational Structure Analysis

In the molecular photo-ionization and photo-excitation processes, the vibrational levels of final electronic states are populated. Such energy transfers from electrons and photons to the nuclear motions can induce the observed vibrational structures in the UPS, XPS, XAS and AES spectra. It is the vibrational structure (also called vibrational progression) that intrinsically determines the line shapes and line widths of the spectral features. By analyzing the vibrational structures, the information of involved electronic state potential curves, electronic configurations, state lifetimes and nuclear dynamics can be obtained.

Under the Born-Oppenheimer approximation, the vibrational transition rate between two electronic states can be evaluated using the Franck-Condon principle, which says the vibrational transition rates (Franck-Condon factors) can be calculated as the squared integral of initial and final vibrational wave functions, $\left|\left\langle \psi_i \mid \psi_f \right\rangle\right|^2$. As shown in Figure 4.1, being an example of general mean-

ing, in the cases of harmonic potentials, the magnitudes of the Franck-Condon factors and the vibrational progression are related to the equilibrium bond length displacement S.

In actual cases, the electronic potential curves are more complex than harmonic potential. In some cases, the Morse potential and Lennard-Jones potential can be good approximations for some potential curves with bonding character, and they have analytical forms of vibrational wave functions. But most of the potential curves do not have analytical forms of potential shapes and vibrational wave functions. Especially, in solving the problems of wave packet propagation on repulsive potentials, within large bond distance or between potential wells, analytical methods are completely not applicable. Hence, methods that can numerically solve the molecular nuclear motion Schrödinger equation and obtain the vibrational wave functions are needed for detailed vibrational structure analysis of general potential surfaces.

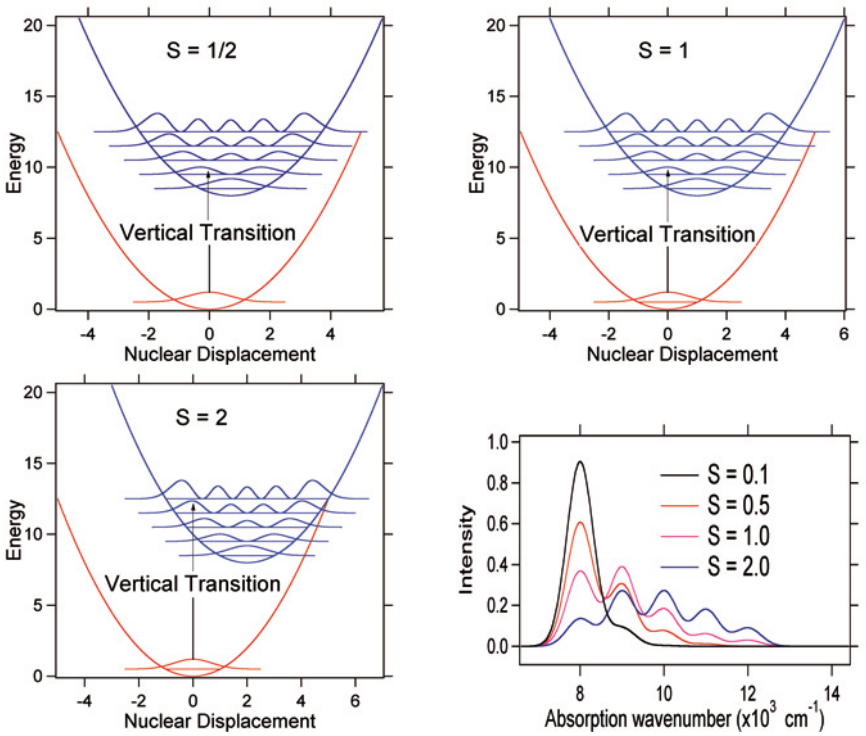

Figure 4.1: Franck-Condon Factors and vibrational transition progressions of harmonic potentials. S is the separation between the equilibrium points of two potential curves. The vibrational transition progression of $S = 0.1$, and the magnitudes of vibrational wavefunctions, $|\psi(r)|^2$, are also shown [15].

4.1.1 Discrete Variable Representation (DVR) Method

DVR (Discrete Variable Representation) method [16] is an efficient numerical method that can solve vibrational levels and wave functions for low-dimensional systems, for example, the diatomic molecules and triatomic molecules. In this method, the discrete variable representation (also called grid point representation) is used to evaluate the molecular nuclear Hamiltonian matrix in a very simple and efficient way.

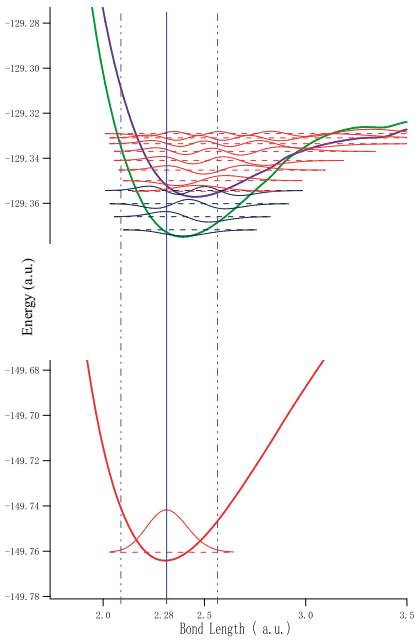

Figure 4.2: Numerical potential curves and vibrational wave functions of O_2 ground state and core-ionized states. The vibrational waves functions are solved by DVR method.

Conventionally, the matrix elements of the Hamiltonian have to be evaluated by calculating the integrations of matrix elements $H_{nm} = \langle\phi_n|\, T + V\,|\phi_m\rangle$ upon the basis set wave functions ϕ_n and ϕ_m. This calculation procedure is time-consuming and it heavily depends on the choice of basis sets. In DVR method, for one-dimensional systems, e.g. diatomic molecules, the kinetic energy operator and potential energy operator of nuclear Hamiltonian can be evaluated using Eq. 4.1 and Eq. 4.2.

In these formulas, $T_{ii'}$ is the kinetic energy operator matrix element corresponding to the grid point numbers i and i'. $V_{ii'}$ is the potential energy operator matrix element, $V(x_i)$ is the potential energy value at bond length x_i. The grid points on bond length (x_i) are uniformly spaced with the interval of Δx. m_1 and m_2 are atomic masses, and m is the reduced mass. The Hamiltonian generated in this way is quite "sparse", which means that it has very small contribution on the non-diagonal matrix elements ($i \neq i'$). It takes much less computation steps to diagonalize Hamiltonian and solve the vibrational wave functions.

$$T_{ii'} = \frac{\hbar^2}{2m\Delta x^2}(-1)^{(i-i')} \begin{cases} \pi^2/3, & i = i' \\ \frac{2}{(i-i')^2}, & i \neq i' \end{cases} \tag{4.1}$$

$$V_{ii'} = \delta_{ii'} V(x_i) \tag{4.2}$$

$$x_i = i \times \Delta x \tag{4.3}$$

$$m = \frac{m_1 \cdot m_2}{m_1 + m_2} \tag{4.4}$$

In Papers **I** and **II**, this method was applied to obtain the ground state, core-ionized states and double-valence-hole Auger final states' vibrational wave functions of the O_2 molecule. In Figure 4.2 the numerical ground state, core-ionized states potential curves and vibrational wave functions of O_2 are shown.

4.1.2 Vibrational Analysis for Auger Electron Spectroscopy

The Franck-Condon principle is valid in most cases of vibrational structure evaluation for core-level and valence-level photoemission spectra. However, in the vibrational analysis and line shape simulations of Auger electron spectrum (AES and RAS), this principle is not valid anymore and additional aspects have to be considered.

In the normal Auger electron emission process there are three kinds of electronic states being involved, the ground state, core-ionized states and final doubly charged states. Quite commonly, as shown in Papers **I** and **II**, the final doubly charged states are closely lying, and potential curve avoided-crossing of electronic states with same symmetries frequently happens. In avoided-crossing, the electronic configurations, Auger transition rates (from core-ionized states to final doubly charged states) are exchanged. Hence, dramatic Auger transition rate variations upon molecular geometries can be observed around the avoided crossing points. So, when the diabatic (or non-adiabatic, avoided crossing) potential curves is applied, in order to take the bond length dependence of Auger transition rates into account, Eq. 4.5 has to be used in the calculation of Auger emission vibrational transition rates. This is especially important when the avoided crossing happens in the Franck-Condon region.

$$I = |\langle f| M_F |n\rangle|^2 \tag{4.5}$$

$$M_F = \sqrt{2\pi}\langle \psi_F| H - E |\psi_N\rangle \tag{4.6}$$

In Eq. 4.5, M_F is the Auger decay transition rate from electronic intermediate state N to electronic final state F. It could have strong bond length dependence when avoided crossing happens. $|n\rangle$ and $|f\rangle$ are the vibrational wave functions, $|\psi_N\rangle$ and $|\psi_F\rangle$ are the electronic wave functions of intermediate state and final state.

The necessity of applying this formalism was proven by the works of Kasper *et al.* [17], Piancastelli *et al.* [18, 19], Sorensen *et al.* [20] and Papers **I** and **II**.

Secondly, in the simulation of the normal Auger transition line shapes, the "one-step" model [21, 22] has to be used rather than the "two-step" model [23], which was conventionally thought to be a good description of the normal Auger emission process. The "one-step" model says the photoionization process (from ground state to core-ionized state) and the Auger decay process (from core-ionized state to final doubly-charged state) are one coherent process. In the molecular Auger electron spectrum, the "one-step" model further describes the interferences between Auger transitions with common final vibrational level but via different intermediate vibrational levels. This is called LVI (Lifetime Vibrational Interference) theory when no PCI interaction was involved. With PCI interaction, a "one-step" model, MAPCI (Molecular Auger Post Collision Interaction) theory should be applied, which was developed in Paper **II** and further discussed in Paper **III**. These theories will be discussed in detail in the later sections.

4.2 Ultraviolet Photoelectron Spectroscopy (UPS)

Valence electrons play the most important role in matter condensation and formation of molecules and solids. Investigating the valence electron structures is crucial for the understanding of the chemical properties, structures and electron transfer characters of matters. UPS technique (including ARUPS) is the standard technique used to study the valence electron characters. In this technique, the electrons on different valence orbitals are photoionized by VUV light (or even higher energy in practice). According to the Einstein's photoelectronic effect principle,

$$E_{kin} = h\nu - E_{bin}, \tag{4.7}$$

the binding energy E_{bin} of the valence electrons can be derived by measuring the photoelectron kinetic energy E_{kin} given a well defined photon energy $h\nu$.

4.2.1 Vibrational Progression in UPS of Free Molecules

In the UPS spectrum of free molecules, the bonding characters of valence orbitals can be obtained by analyzing the observed vibrational progressions and line widths. As shown in Fig. 4.1, according to the Franck-Condon principle, the vibrational transition progression pattern is related to the equilibrium geometry difference between the initial and final states, while the equilibrium ge-

ometry difference is in turn determined by the electronic configurations (electron populations).

The total bonding character of a molecule is actually the add-up of the contributions of all bonding, non-bonding and anti-bonding orbitals. When molecules are at the equilibrium geometry of the ground state, taking away (photo ionization) an electron from a bonding orbital will render the total electronic configuration with anti-bonding characters, and change the equilibrium geometry of the final state to longer bond length. On the other side, taking away an anti-bonding orbital electron can add bonding characters to the total electronic configuration, and then the equilibrium geometry of the final state will exhibit shorter bond length. As a natural result, ionization of a non-bonding electron can result in a final state equilibrium geometry with bond lengths similar to those of the initial state. So the UPS spectral components for electrons ionized from strong bonding orbitals will exhibit long vibrational progressions and have the maximum at higher vibrational levels. The components for electrons ionized from strong anti-bonding orbitals have narrower vibrational progressions.

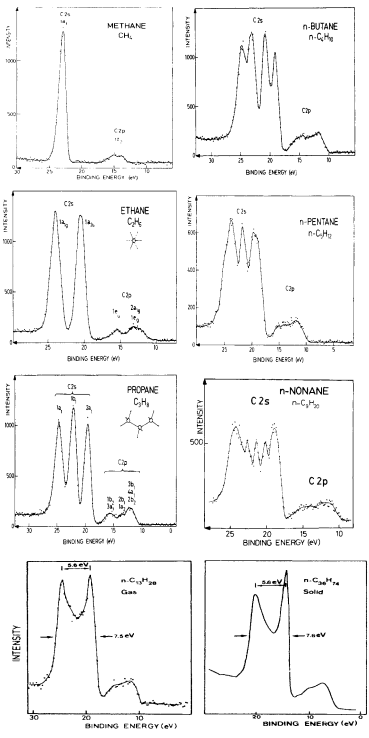

Figure 4.3: The valence level photoemission spectra of methane, ethane, propane, butane, pentane, nonane, $C_{13}H_{28}$ and $C_{36}H_{74}$ [24, 25].

4.2.2 2*s* Bands in Photoemission of Organic Molecules

As mentioned at the beginning of this section, the valence electrons play the main role in molecular bonding. In a simple picture, the bond formation is due to the overlapping of atomic valence orbitals. Obviously, an outer atomic valence orbital has larger overlaps with the orbitals of the other atoms and pays more contributions to the formation of molecular bonds, while an inner atomic valence orbital, has smaller overlaps and will contribute less to the molecular bonds. In the UPS spectrum or valence level XPS spectrum, these electrons belonging to different valence shells can be observed forming separated bands.

The well known examples are the valence photoemission spectra of organic molecules and polymers.

Carbon atom has three electronic shells, 1s, 2s and 2p shells. The 1s shell is a core orbital shell which does not take part into the molecular bonding formation. The 2s is an inner valence shell, and it contributes less than the outer 2p valence shell to the molecular bonding. So, as systematically shown by Pireaux *et al.* [24, 25], in Figure 4.2.1, in the valence photoemission spectrum of organic molecules, the spectral components corresponding to 2s valence hole show small vibrational progressions indicating the non-bonding character of 2s orbitals. At the same time, the energy shifts of 2s photoemission components reflects the chemical environments and the number of these components equals to the number of carbon atoms.

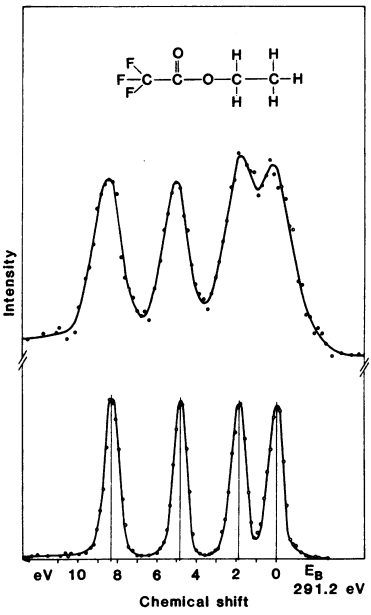

Figure 4.4: Electron spectroscopy for chemical analysis (ESCA) [26]. The C1s XPS spectral features shows the energy shifts indicating the different chemical environments.

4.3 X-ray Photoelectron Spectroscopy (XPS)

To reach the deep-lying core-level electrons of atoms and molecules, high energy photons, e.g. XVUV, X-ray, hard X-ray, are used in the photoemission technique. This kind of technique, specifically called "XPS", treats the electrons on the 1s orbitals for the elements in the second row of periodical table, or on the 1s and 2p orbitals for third row elements, and so on.

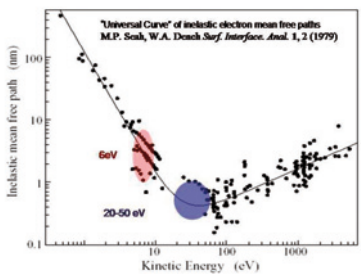

Figure 4.5: The universal curve of electron inelastic scattering mean free path [27].

This technique has several advantages. Firstly, as a natural result of significant binding energy differences for the core-level electrons of different elements, XPS is an element-specific method. Secondly, at variance with valence electrons, core electrons do not participate in bond formation, and are localized around the nuclei, so XPS is a site-specific technique. Thirdly, when atoms bond to each other and form

molecules, charge redistribution between atoms and valence configuration changes will happen. In this case, the induced electric field can result in energy shifts of the core-level orbitals. As shown in Figure 4.4, different bonding orders and bonding environments lead to different energy shifts for the same element, which is called as "chemical shift". So, as a chemical-sensitive technique, XPS technique is also called ESCA (Electron Spectroscopy for Chemical Analysis) [28]. In surface physics, by using synchrotron radiation, the photoelectron kinetic energy can be controlled, and the mean free path of electron inelastic scattering can be modified. As shown in Fig. 4.5, with a kinetic energy about 50 eV, only the electrons from a few atomic layers on the top of surface can be detected. In this sense, XPS is also a surface sensitive method.

However, because of the ultra-short lifetime of a core-hole state, which is in the order of femtosecond ($1\ fs = 1 \times 10^{-15}$ second), the lifetime energy broadening of a single vibrational component in XPS spectrum is around 0.1 eV. This makes the vibrational analysis difficult if the vibrational interval of core-ionized state is too small.

4.4 X-ray Absorption Spectroscopy (XAS)

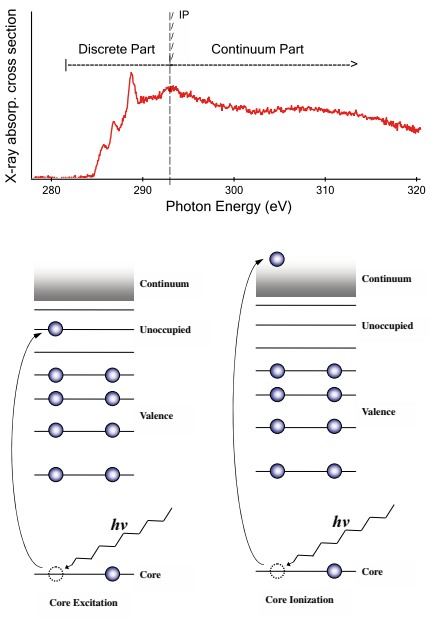

Figure 4.6: The two parts of general XAS spectrum and the main processes involved.

In X-ray Absorption Spectroscopy techniques, by measuring the X-ray attenuation or the secondary products, core-level electron excitation and ionization cross sections due to X-ray photon absorptions are obtained. In the XAS spectrum there are two parts in principle, as shown in Figure 4.6. One part is called discrete part in which spectral structures are evident. It is produced by the photo-excitation of core-level electron to the discrete unoccupied orbitals below the ionization threshold. The other part is called continuum part. Since it is mainly due to the photoionization process, no obvious structures can be found. Nowadays, most of XAS spectra are obtained by measuring the secondary products due to core-hole creation, e.g. the Auger electrons, photo-ions, x-ray fluorescence and so on. Depending on the detail of techniques and products, different names are used. For

example, in the TIY technique the yields of all kinds of ions are measured, while in the "partial ion yield" technique only the yield of a specific ion is counted.

The cross section of X-ray absorption can be calculated according to Fermi's golden rule,

$$\sigma_{XAS} \propto |\langle f| \vec{e} \cdot \vec{p} \, |i\rangle|^2 \, \rho\left(E_f\right) \cdot \delta\left(E_f - E_i - h\nu\right). \tag{4.8}$$

In this equation, $|i\rangle$ is the wave function of initial ground state, $|f\rangle$ is the wave function of final core-excited states, $\vec{e}$ is the unit vector of the radiation electric-field vector, $\vec{p}$ is the linear electron momentum operator, $\rho\left(E_f\right)$ is the density of states for final states. Eq. 4.8 shows that the X-ray absorption process is a "dipole interaction" between the photon and electrons. Hence, the selection rule governing is called "dipole selection rule". It says that, the angular momentum difference between initial state and final state should be $\Delta l = \pm 1$, which means that for the electron excitation from a $1s$ orbital, the final state can only be a p type orbital. Furthermore, the scalar product $\vec{e} \cdot \vec{p}$ indicates the dependence of cross section σ_{XAS} on the angle between the photon electric-field vector and the molecular orientation. In studying the free molecules, with angle-resolved photoion-yield spectroscopy technique, the angular dependence information and symmetries of molecular unoccupied orbitals can be obtained [29].

4.4.1 Near Edge X-ray Absorption Fine Structure (NEXAFS)

In surface physics, a XAS technique focusing on the energy range about 30 eV above absorption edges, which is called NEXAFS, is widely used to study the surface-adsorbate systems. Since all the atoms and molecules on a surface are experimentally fixed in space, by analyzing the angular dependence of the discrete part of NEXAFS spectra, the adsorbate orientations and adsorbate-surface interactions can be precisely investigated [30].

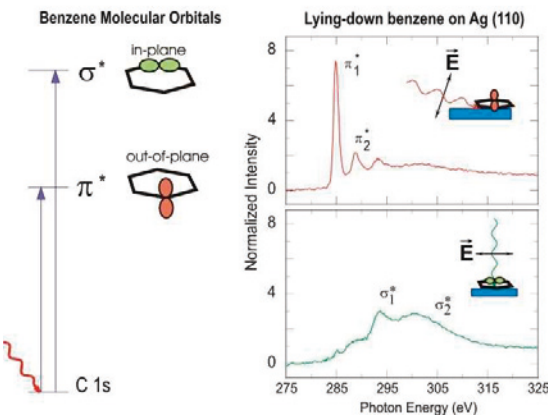

Figure 4.7: The dependence of NEXAFS cross section on the angle between photon electric-field vector and adsorbed molecule orientation. [30]

The physisorption of benzene on metal surface is a good example. As shown in Figure 4.7, for the excitations from $1s$ core level orbital to the p type unoc-

cupied orbitals, by changing the angle between the photon electric-field vector and the molecular orientations, different types of unoccupied orbitals can be chosen to be populated.

The p type atomic orbitals can form π type and σ type molecular orbitals. The π type orbitals are out of the molecular skeleton plane, and the σ type is in plane. So, when the photon electric-field vector is perpendicular to the molecular plane, the excitation cross sections to π^* bond reach the maxima and no σ^* excitation can be seen in the NEXAFS spectrum, but when the photon electric-field vector is in the molecular plan, only the σ^* excitation can be observed in spectrum.

On beamline I511, MAX-lab, NEXAFS experiments by measuring Auger electron yield can be performed using the Scienta SES-R4000 hemispherical electron energy analyzer, and the sample can be rotated to reach different angles between the electric-field vector and the sample surface.

4.4.2 Density Functional Theory (DFT) method

In the discrete part of NEXAFS spectrum, intense and sharp features can be found, and by the help of the excitation angular dependence, some of the core excitation channels of highly symmetric systems can be experimentally assigned. However, dealing with a general systems without high symmetries, the aid of theoretical simulations is crucial. Density Functional Theory (DFT) [31, 32] is one of the most popular theoretical methods being widely applied in quantum chemistry and solid states physics. TD-DFT (Time Dependent Density Functional Theory) method is one of the most important development of DFT method. It expands the DFT method into the time scale and gives the ability of calculating the excited states. Nowadays, this method has become one of the most important tools to investigate the chemical reaction, optical properties of condensed matter, surface and molecule photo-chemistry and so on. In our work, Paper **1** and **2**, TD-DFT [33–35]method was used to simulated the angular resolved NEXAFS spectra. Here, I will just briefly make a conceptual introduction of DFT method.

In a traditional many-body electronic structure calculation method, the essential variable is the multi-electron wave functions $\Psi = \Psi(\mathbf{r}_1, ..., \mathbf{r}_N)$. To obtain these multi-electron wave function and the energies, we have to solve a multi-electron Schrödinger equation,

$$\begin{aligned} H\Psi &= E\Psi \\ &= [T + V + U]\,\Psi \\ &= \left[-\sum_i^N \frac{\hbar^2}{2m}\nabla_i^2 - \sum_i^N V(\mathbf{r}_i) + \sum_{i<j} U\left(\mathbf{r}_i, \mathbf{r}_j\right) \right] \Psi, \end{aligned} \tag{4.9}$$

where T is the kinetic energy operator, V is the single electron potential energy operator and U is the electron-electron interaction operator.

However, in DFT method, the key variable is the electron density $n(\mathbf{r})$,

$$n(\mathbf{r}) = N \int d^3 r_2 \int d^3 r_3 ... \int d^3 r_N \; \Psi^*(\mathbf{r}, \mathbf{r}_2, ..., \mathbf{r}_N) \Psi(\mathbf{r}, \mathbf{r}_2, ..., \mathbf{r}_N), \quad (4.10)$$

while the multi-electron wave function $\Psi(\mathbf{r}_1, ..., \mathbf{r}_N)$ is just a unique functional of the electron density,

$$\Psi = \Psi[n], \quad (4.11)$$

so as the other operators and variables. By taking a non-interacting kinetic energy T_S and a effective potential $V_S = V + U + (T - T_S)$ describing all the interactions that a single electron feels, the total energy can be written into a non-interacting way,

$$E[n] = E_S[n] = \langle \Psi_S[n] | \, T_S + V_S \, | \Psi_S[n] \rangle, \quad (4.12)$$

and the multi-electron many-body problem can be simplified to a series of single-electron problems. The effective single-electron equations are called Kohn-Sham equations,

$$\left[-\frac{\hbar^2}{2m} \nabla^2 + V_S(\mathbf{r}) \right] \phi_i(\mathbf{r}) = \varepsilon_i \phi_i(\mathbf{r}). \quad (4.13)$$

By solving these equations, non-interacting single-electron wave functions ϕ_i can be obtained and further the total electron density n, which determines the total multi-electron wave functions Ψ, can be reproduced simply,

$$n(\mathbf{r}) = \sum_i^N |\phi_i(\mathbf{r})|^2. \quad (4.14)$$

Obviously, in the whole procedure, the most important step is to find a effective potential V_S to "isolate" a single electron from the others. In detail, V_S is expressed as

$$V_S = V + \int \frac{e^2 n_S(\mathbf{r}')}{|\mathbf{r} - \mathbf{r}'|} d^3 r' + V_{XC}[n_S(\mathbf{r})]. \quad (4.15)$$

The most tricky term is the exchange correlation potential, V_{XC}, which includes all the many-body interactions. In the actual applications, different types of potential functionals describing the exchange interactions and correlation interactions are available. They are optimized for different systems and have different performances.

4.5 Auger Electron Spectroscopy (AES)

Auger electron emission process is the main decay process occurring after core-hole creation for low Z elements [1], while the X-ray emission decay (radiative decay) accounts only for about 10% of the total decay events. As shown in

[1] including the second- and third-row elements in the periodic table.

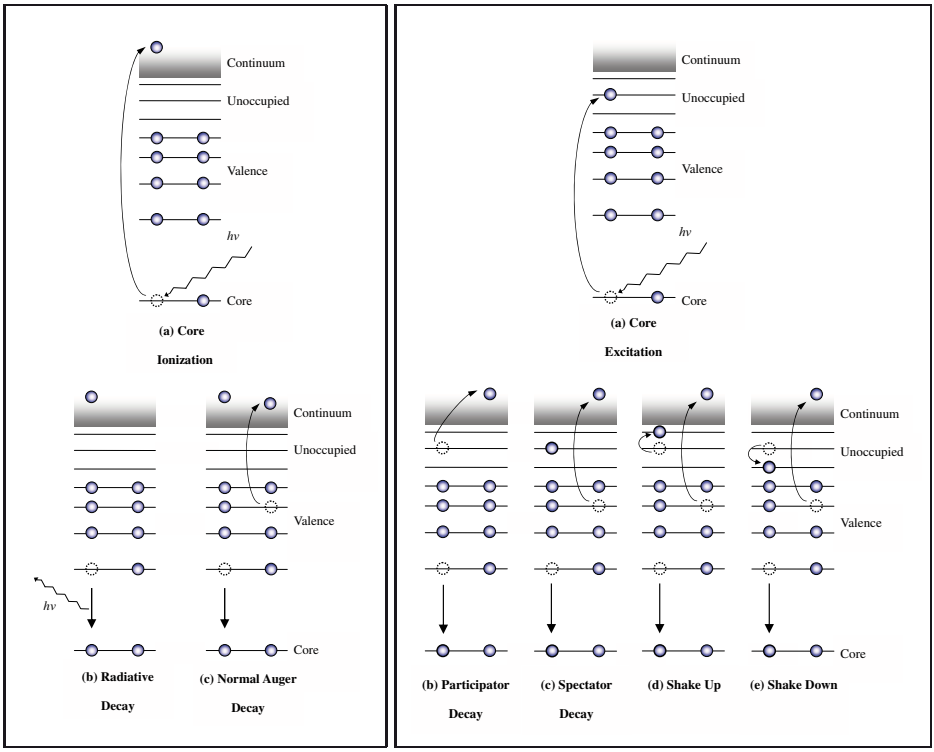

Figure 4.8: Left: Schematic representation of core-level electron ionization and the following decay processes. (a), photo-ionization of core-level electron; (b), radiative decay (X-ray emission) process; (c), non-radiative decay (Auger decay) process. *Right*: Schematic representation of core-level electron excitation and resonant Auger processes. (a), core-level electron photo-excitation process; (b), participator decay; (c), Spectator decay; (d), shake up; (e), shake down.

Figure 4.8, the core-level electron hole can be created non-resonantly (photo-ionization) and resonantly (photo-excitation). In both cases, the core-hole will be filled by an electron coming from outer shells (including the valence orbitals and the populated unoccupied orbitals). At the same time, another electron (the Auger electron) from outer shells will be ejected, which is called Auger electron.

Resulting from the different core-hole states, Auger processes can be divided into two kinds. One is referred as normal Auger process, in which the core-level electron is ionized, and the other is referred as resonant Auger process, in which the core-level electron is excited to unoccupied orbitals. Resonant Auger process can follow two kinds of pathways corresponding to different electronic configurations of the final states. One is called participator decay, as shown in Figure 4.8 (*Right*, b), the electron populating an unoccupied orbital participates in the decay process. Since the final electronic configurations of participator decays are the same as those corresponding with valence electron ionization, the line shape of participator Auger components in the spectra are

very similar to the valence level photoemission spectrum, in which the vibrational structure is quite well defined and peaks are well separated. The other one is called spectator decay, shown in Figure 4.8 (*Right*, c), in which the excited core electron stays on the unoccupied orbital without joining the Auger electron emission process. In spectator decay, the final configurations have two valence holes and one electron on an unoccupied orbital, hence the density of states is much higher than that in participator Auger decay. So the molecular spectator Auger decay spectrum is hard to analyze. Comparing to the participator decay Auger electrons, the spectator decay Auger electrons have lower kinetic energies.

When the core electron is excited to one of the Rydberg states of molecules, which are generally decoupled with valence electron orbitals, "shake up" and "shake down" are two probable satellite processes. They could have considerable cross sections and affect the Auger electron spectra significantly. As shown in figure 4.8 (*Right*, d), for a shake-up process, the excited electron lying on Rydberg orbital can obtain energy from the Auger electron and transit to a Rydberg orbital with higher energy. Consequently, the Auger electron kinetic energy will be lower than that of the normal spectator decay. On the other side, as shown in Figure 4.8 (*Right*, e), the electron on Rydberg orbital can also jump to an orbital with lower energy and transfer energy to the Auger electrons which will have higher kinetic energy.

It can be noticed that the core-level electron photo-ionization and photo-excitation processes can also induce "shake up", in which the valence electrons obtain energies and transit to unoccupied orbitals.

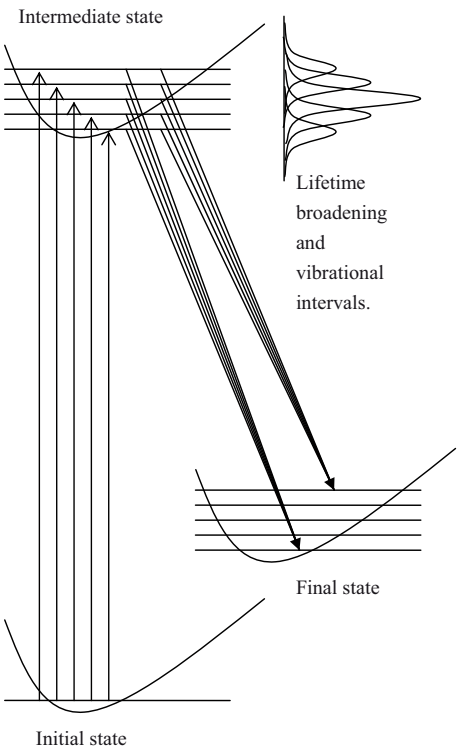

Figure 4.9: Schematic representation of the coherent excitation and the interference of common final state vibrational Auger transition channels via different intermediate vibrational levels.

Lifetime Vibrational Interference (LVI) Effect

The "one-step" model and the "two-step" model [36] have been used to describe the Auger electron emission process (both the resonant and the normal Auger electron emission).

In the "two-step" model, the core-level electron excitation/ionization is treated as independent from the Auger electron emission process. This model is considered as a good description in the case of normal Auger decay process when the photoelectron kinetic energy is higher than the Auger electron kinetic energy [36]. As a contrast, the "one-step" model is based on the unified time-independent resonant scattering theory [22, 36]; it treats the excitation/ionization of core-level electron as a coherently interactive process with the Auger electron emission process. It is a more general theory and more suitable for the description of a resonant Auger process (autoionisation process).

In molecular systems, with the Born-Oppenheimer approximation, the formula of "one-step" model can be expanded into the LVI (Lifetime Vibration Interference) theory [17, 21, 37–39] when the PCI effect is not involved. LVI theory describes the interference between the vibrational Auger decays having common final vibrational state but different intermediate vibrational levels and different intermediate electronic states (the core-excited or core-ionized states), as shown in Figure 4.9.

In LVI theory, the total cross section of Auger decay involving one intermediate electronic state, I_F, is expressed as Eq. 4.16. M_F^{lm} is the Coulomb Auger decay operator matrix element [2] for the Auger electron out going channel lm. D is the dipole operator matrix element representing the core electron photoionization or photo-excitation. $|f\rangle$, $|n\rangle$ and $|0\rangle$ are the vibrational wave functions of the final electronic state, intermediate core-hole state and initial ground state. Γ is the lifetime energy broadening of the core-hole state. $|\Psi_N\rangle$, $\left|\Psi_F^{lm}\right\rangle$ and $\left|\Psi_0\right\rangle$ are the electronic wave functions of intermediate state, final state and initial ground state. E_f and E_n are the vi-

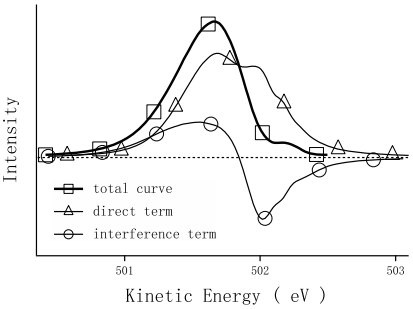

Figure 4.10: Typical shapes of LVI terms with broad photon energy band pass. The total LVI line shape (—□—) is significantly different from the line shape of "Direct Term" (—△—) which equals to the line shape evaluated using "two-step" model.

[2] Auger decay is a Coulomb interaction.

brational level energies of final state and intermediate state.

$$I_F(E_{kin}) = \sum_f \sum_{lm} \left| \sum_n \frac{\langle f| M_F^{lm} |n\rangle \langle n| D | 0\rangle}{E_{kin} - E_n + E_f + i\Gamma/2} \right|^2 P(h\nu) \tag{4.16}$$

$$M_F^{lm} \propto \sqrt{2\pi} \langle \Psi_N | H - E | \Psi_F^{lm} \rangle \tag{4.17}$$

$$D \propto \langle \Psi_N | \hat{r} | \Psi_0 \rangle \tag{4.18}$$

The Eq. 4.16 can be further expanded into a detailed form. As the expanded form of Auger transition cross section of decay channel *lm*, in Eq. 4.19, two terms can be obtained. The first term is called the "Direct Term". It is simply a summation of the vibrational transition intensities with including the core-hole lifetime broadening. If the bond length dependence of Auger transition rate is neglected, this term is then simplified as the summation of Franck-Condon factors with convolution of Lorentzian function which has a FWHM of core-hole lifetime broadening. The second term is called the "Interference Term". It represents the interferences between the vibrational Auger transitions having the same final vibrational state but different intermediate vibrational levels.

$$I_F^{lm}(E_{kin}) = \sum_f \left| \sum_n \frac{\langle f| M_F^{lm} |n\rangle \langle n| D | 0\rangle}{E_{kin} - (E_n - E_f) + i\Gamma/2} \right|^2 P(h\nu) \tag{4.19}$$

$$= \Bigg\{ \underbrace{\sum_f \sum_n \frac{(\langle f| M_F^{lm} |n\rangle \langle n| D | 0\rangle)^2}{[E_{kin} - (E_n - E_f)]^2 + \Gamma^2/4}}_{Direct\ \ Term}$$

$$+ \sum_f \sum_{m \neq n} \Bigg[\langle f| M_F^{lm} |n\rangle \langle n| D | 0\rangle \langle f| M_F^{lm} |m\rangle \langle m| D | 0\rangle$$

$$\underbrace{\times \frac{\{[E_{kin} - (E_n - E_f)][E_{kin} - (E_m - E_f)] + \Gamma^2/4\}}{\{[E_{kin} - (E_n - E_f)][E_{kin} - (E_m - E_f)] + \Gamma^2/4\}^2 + (E_n - E_m)^2 \times \Gamma^2/4} \Bigg]}_{Interference\ \ Term}$$

$$\Bigg\} P(h\nu) \tag{4.20}$$

Usually, if the core-hole lifetime broadening is comparable to the interval of intermediate state vibrational levels, the interference term will change the Auger transition band shape significantly comparing with the line shape obtained by "two-step" model, as shown in Figure 4.10.

5. Results and Discussion

5.1 Synchrotron Radiation Study of Free Molecules

5.1.1 Auger Electron Spectroscopy of Free Molecules

Our group has focused on the core-hole induced and involved molecular electronic dynamics, in Papers **I**, **II**, **III** and **IV**, and nuclear dynamics, in Paper **3** and **4**. Auger electron emission process is the main decay channel for light elements after the core-hole creation. In the intensive studies of Auger process, since 1920, the "one-step" model is one of the most important conceptual advances. In a general way, it successfully describes the resonant Auger electron emission and normal Auger electron emission processes as coherent phenomena. In Paper **I**, taking the diatomic open-shell molecules O_2 as model system, we started with trying to understand traditional questions by applying the "one-step" model in a detailed way. In Papers **II**, **III**, based on the deep understanding and the development of new theory and methods, we are exploring new phenomena. An attempt to understand the character of larger molecules was performed in Paper **IV**.

Application of "One-Step" Model

O_2 is the showcase for open-shell molecules. Its normal Auger spectrum is a traditional topic. In Paper **I**, the molecular version of "one-step" model, LVI (Lifetime Vibrational Interference) theory was applied to make the quantitative assignment of the normal Auger spectrum with the help of *ab initio* CI calculation, numerical vibrational wavefunction calculation and curve-fitting procedure.

With the *ab initio* CI method described by Fink *et al.* [41], the potential curves of O_2 ground state, core-ionized intermediate states and doubly charged final states are calculated. At the same time, the Auger decay transition rate curves upon bond length are obtained using one-center approximation for all the final states considered. The Auger transition line shapes were calculated using Eq. 4.19, which includes the bond length dependence of Auger transition rates. The obtained Auger line shapes are fitted to the experimental data [40] in a curve-fitting procedure to correct the errors of calculated state energies and Auger transition rates. In Figure 5.1, the energy corrected avoided-crossing core-ionized state and doubly charged final state potential curves are shown. The quantitative assignment of the O_2 normal Auger spectrum, including the

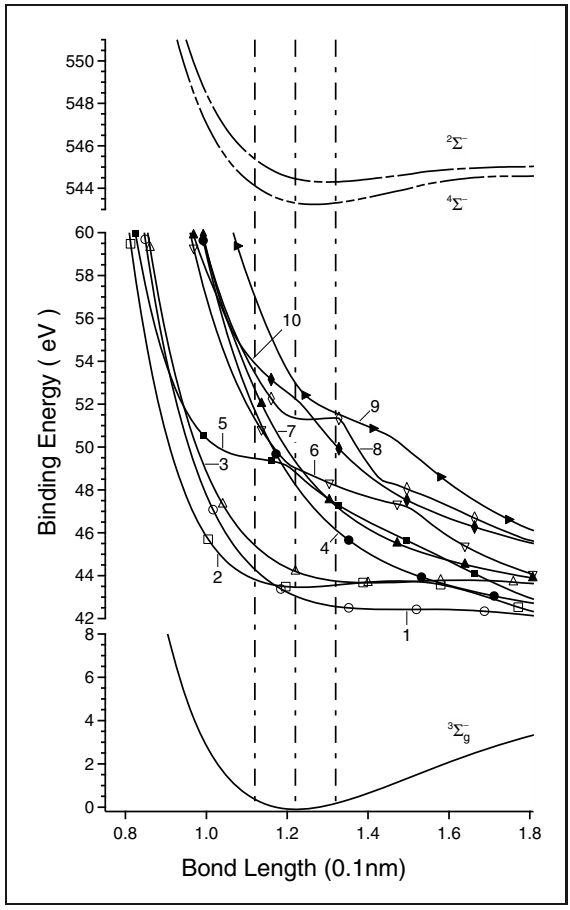

Figure 5.1: The ground state potential curve, curve-fitted core-ionized state potential curves and the curve-fitted triplet final state potential curves. Different final states are labeled with different markers: (—○—) for 1 $^3\Delta_u$, (—□—) for 2 $^3\Pi_g$, (—△—) for 3 $^3\Sigma_u^-$, (—●—) for 4 $^3\Delta_g$, (—■—) for 5 $^3\Pi_u$, (—▽—) for 6 $^3\Pi_u$, (—▲—) for 7 $^3\Sigma_g^-$, (—◊—) for 8 $^3\Pi_u$, (—►—) for 9 $^3\Sigma_g^-$ and (—♦—) for 10 $^3\Sigma_g^-$.

Auger transition line shapes, energies, and Auger transition rates is shown in Fig. 5.2.

In this work, firstly, the importance of "one-step" model is underlined. In the curve-fitting procedure, the line shape simulation is crucial. Using the LVI formalism, the interference between vibrational transitions with common final state but via different intermediate states are included. Secondly, the "one center approximation" was proven to be effective. The calculated Auger transition rates fit well will the curve-fitted Auger transition rates. Thirdly, including the bond length dependence of Auger transition rates in the evaluation of Auger line shapes with avoided-crossing final state potential curves is shown to be rather important.

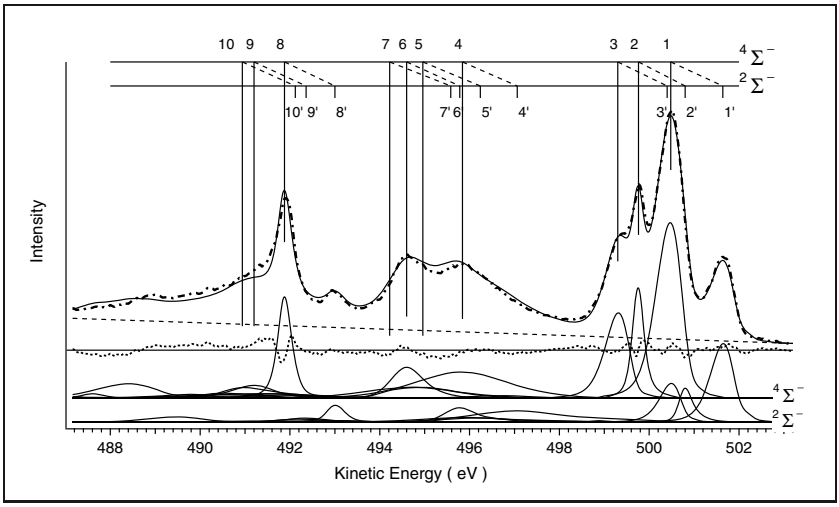

Figure 5.2: The result of curve-fitting to the experimental O_2 normal Auger spectrum [40] (— · —). The curve-fitting is based on theoretical simulated Auger decay LVI line shapes. The Auger decay components having common final states are connected by the dashed lines and are similarly labeled (e.g. 1 and 1'). The solid line is the total sum of the Auger decay line shapes.

Development of "One-Step" Model

In recent years, with the advances of synchrotron radiation and data analysis technique, the vibrational structures of molecular normal Auger spectra have become a hot topic [42–44]. In these studies, the same as in Paper **I**, "one-step" model, LVI theory plays the crucial role in simulating molecular Auger line shapes. However, always in treating the PCI effect, the approximations that have been used are not satisfactory.

Having the detailed quantitative assignment of O_2 normal Auger spectrum which is free from PCI effect as a good model system, in Paper **II**, a new molecular "one-step" model, MAPCI (Molecular Auger Post Collision Interaction) theory was developed. In Paper **III**, the shape resonance affected MAPCI effect was studied.

In theory, the formula of MAPCI was started from the time-independent resonant scattering theory of Åberg *et al.* [45]. Under the Born-Oppenheimer approximation and giving that the PCI effect does not influence the Auger transition rate, and neglecting the double-ionization channel, the MAPCI formula is obtained,

$$\frac{d\sigma_{\mathbf{F}}}{d\epsilon_A} \propto \left| \sum_n \langle \epsilon|\tau'_n\rangle \langle f|M_{FN}|n\rangle \langle n|D_{N0}|0\rangle \right|^2 . \tag{5.1}$$

where

$$\langle \epsilon|\tau'_n\rangle = \int \frac{\langle \epsilon|\tau_n\rangle}{E_0 + h\nu - E_n + \tau_n + i\,\Gamma/2}\, d\tau_n \tag{5.2}$$

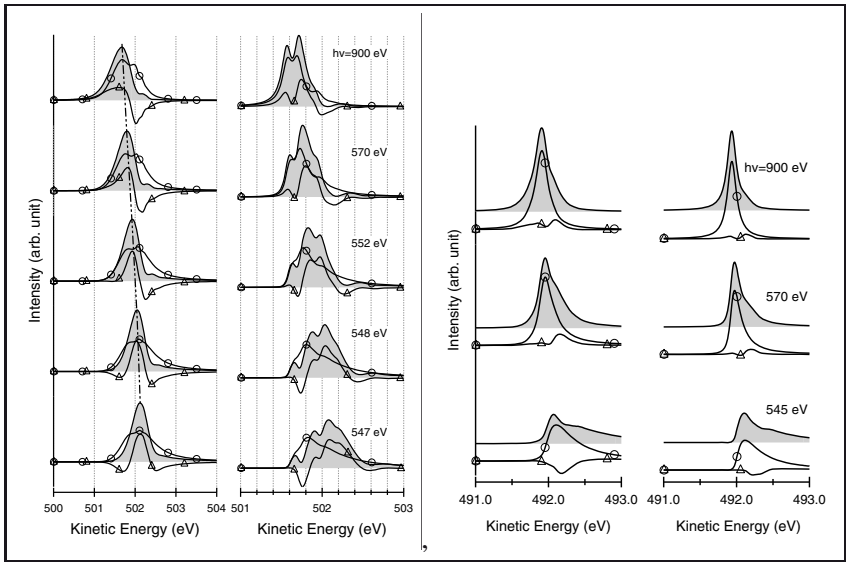

Figure 5.3: Left:"molecular PCI" effect. The photon energy dependent evolutions of kinetic energies and line shapes of total Auger transition band and single final vibrational transition band. *Right:* "atomic-like PCI" effect. The photon energy dependent evolutions of kinetic energies and line shapes of total Auger transition band and single final vibrational transition band. The filled area is the total Auger line shape curve, the labeled curves represent the "Direct Term"(◯) and the "Interference Term" (△) in Eq. 5.3.

is the PCI transition amplitude. ϵ_A is the final state Auger electron kinetic energy. ϵ is the final state photoelectron kinetic energy and τ_n is the intermediate state photoelectron kinetic energy. $M_{FN} = \langle\psi_{\epsilon_A F}|H - E|\psi_N\rangle$. and $D_{N0} = \langle\psi_{\tau_n N}|V|\psi_0\rangle$ are the matrix elements describing the Auger decay process and dipole ionization process. E_0 and E_n are energies of ground and intermediate states. Γ is the lifetime broadening of intermediate state.

In the further expansion,

$$\frac{d\sigma_{\mathbf{F}}}{d\epsilon_A} = \underbrace{\sum_n \left|\langle\epsilon|\tau'_n\rangle\langle f|M_{FN}|n\rangle\langle n|D_{N0}|0\rangle\right|^2}_{\text{direct term}} + \underbrace{\sum_{n\neq m}\Big(\langle\epsilon|\tau'_n\rangle\langle f|M_{FN}|n\rangle\langle n|D_{N0}|0\rangle\Big)^*\Big(\langle\epsilon|\tau'_m\rangle\langle f|M_{FN}|m\rangle\langle m|D_{N0}|0\rangle\Big)}_{\text{interference term}}, \tag{5.3}$$

it can be clearly seen that this theory describes the interference between the PCI amplitude of Auger vibrational transition channels having common final state f but different intermediate vibrational level n.

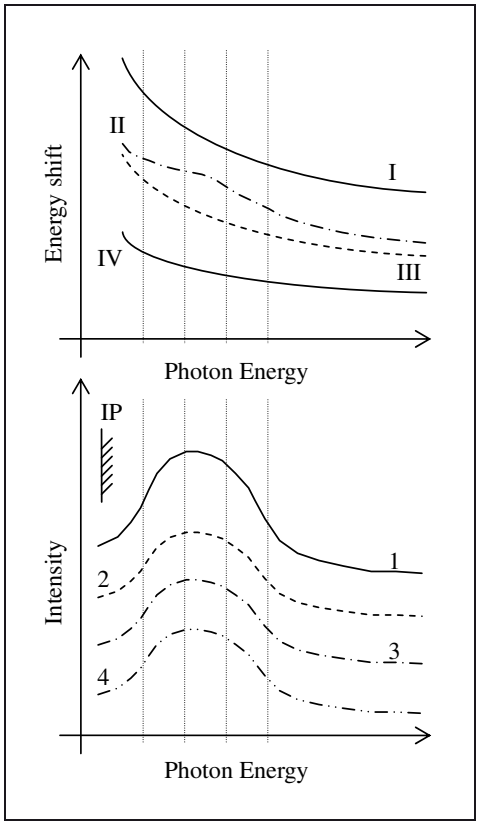

Figure 5.4: A qualitative picture of shape resonance affect MAPCI energy shift above ionization potential (IP). *Up*: the MAPCI energy shift curves of unaffected (III) and affected (II) cases, the atomic maximum (IV) and gravity center (I) PCI shift are shown for comparison. *Down*: the intensity variation of resonance cross section (1), population branching ratio or high vibrational levels ($n \geq 1$)(2), amount of interference (3) and "molecular PCI" character (4).

In experiments, the O_2 near threshold normal Auger spectra were obtained. Detailed study of the energy shifting and line shape evolutions of the spectral features showed that different peaks have different photon energy dependent behaviors. These effects were proved by theoretical simulations as a phenomenon reflecting the amount of interference effect involved.

As shown in Figure 5.3, there are two extreme cases, "molecular PCI" effect and "atomic-like PCI" effect. In "molecular PCI" effect, the interference between vibrational transition channels are much stronger because of the comparable intensities of involved transitions. It shows large energy shifting and small line shape variation upon the changing of photon energy. In the "atomic-like PCI" effect, since one single transition channel is dominant, the interference involved is much weaker. Then, it appears more like the atomic case, in

which, the energy shift of peak maximum is small and severely asymmetric line shape rises.

In the shape resonance region, the MAPCI effect is further affected because of the vibrational branching ratio changing of core-ionized state. This was described in Paper **III**, in which the NO molecular near threshold normal Auger was studied. The branching ratio increasing of higher vibrational levels of core-ionized state has been observed for several molecules [46, 47] in the shape resonance region, as shown in Fig. 5.4. The shape resonance can induce the enhancement of interference, and increasing of "molecular PCI" character.

5.1.2 Combined Techniques Study of Poly-atomic Molecules

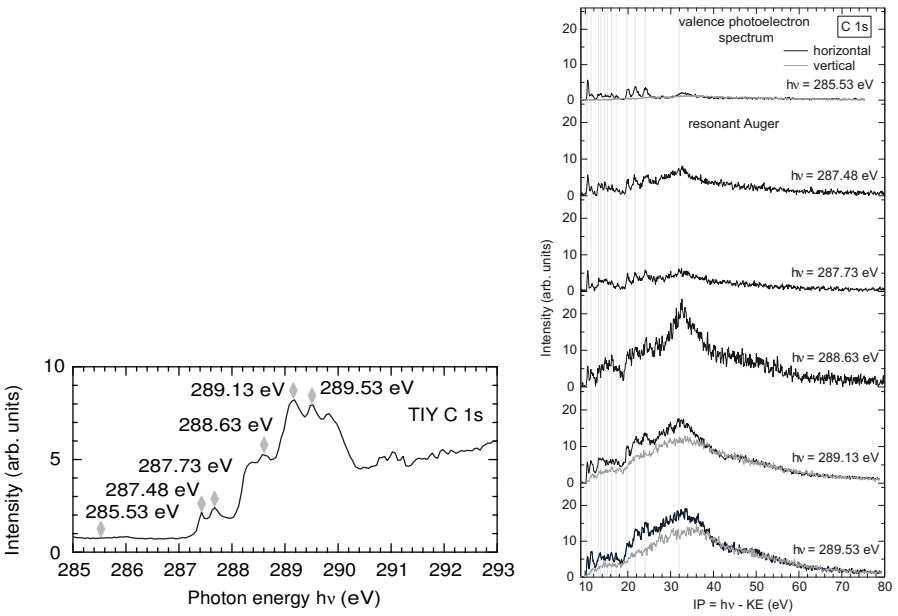

Figure 5.5: Left: TIY around the C K-edges. The arrows mark the photon energy values at which resonant Auger spectra were recorded. *Right*: RAS at different photon energies. The labels "horizontal" and "vertical" refer to spectra taken with the polarization vector in the horizontal and the vertical plane respectively.

Together with small open-shell molecules, our group is also interested in poly-atomic molecules, i.e., methyl oxirane, N_2O, CO_2 and aliphatic CH_3-X (X=Br, NH_2 and so on) compounds. In Paper **IV**, the methyl oxirane is studied with XPS, TIY, AES and RAS (Resonant Auger Spectroscopy) combined experimental techniques and, theoretically, LDOS (Local Density Of States) method and "independent particle" model.

Because of the large lifetime broadening, the O1*s* XPS of methyl oxirane is structureless and vibrational structure could not be resolved. The assignment of

C1*s* XPS spectrum was performed by comparing with *ab initio* result of Mulliken atomic charge distribution. According to the principle of chemical shift, the CH_3 radical has the largest amount of negative charge and correspondingly the lowest binding energy, while the CH radical has the largest amount of positive charge and the highest binding energy.

The XAS (X-ray Absorption Spectroscopy) of methyl oxirane is studied with TIY method. Due to the smaller life time broadening, the resonances to unoccupied orbitals are precisely determined around the C K-edge. The assignment of the C K-edge XAS can be obtained according to the chemical shifts of different carbon atoms. As mentioned in previous theoretical studies [48, 49], the unoccupied orbitals of methyl oxirane are mixed with Rydberg orbitals. Our resonant Auger spectra also confirmed this point. In figure 5.5 the resonant Auger spectra show a preferential spectator decay, which is a sign for non-coupling of core-excited virtual orbitals with valence orbitals. The similarity between spectral line shapes of RAS at different photon energies with the normal Auger spectra indicates the non-bonding character of all Rydberg mixed excitations. The RAS of the O K-edge also showed strong Rydberg orbital mixing feature, based on the same argument for the C K-edge.

LDOS calculation based on SCF methods and independent particle model successfully explained the features of spectator decay channels in RAS and the spectral line shape of normal Auger spectra.

5.2 Epoxy Molecules on Si (100) surface

The chemisorptions of epoxy molecules (ethylene oxide, methyl oxirane, cis-dimethyl oxirane, trans-dimethyl oxirane) on single- and multi-domain Si (100) surfaces have been investigated by our group. In Paper **V** and **VI**, the chemisorption bonding geometries and characters of methyl oxirane and ethylene oxide are investigated by XPS, UPS and NEXAFS techniques. In Paper **VII**, the chiral property of the adsorbed methyl oxirane enantiomers is searched by using CDAD technique.

5.2.1 Chemisorption of Methyl Oxirane

Methyl oxirane is an important chemical for polymer industry and medical industry. The oxirane three-membered ring characterizes the molecule with ring-opening reaction possibility and chiral geometry. As shown in Figure 5.6, there are two possible chemisorption bonding geometries for methyl oxirane on Si (100).

To clarify the bonding geometries at room temperature, C 1*s*, Si 2*p* core level and valence level photoemission spectra were measured at different electron emission angles (45° and normal emission angle). NEXAFS spectra around the C K-edge were measured for different angles (0°, 45° and 90°)

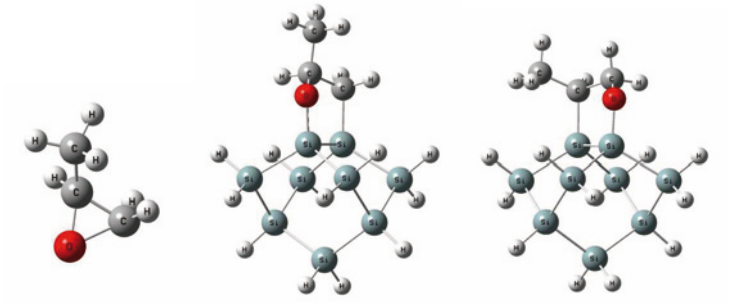

Figure 5.6: The gas phase molecular structure (a), and two possible chemisorption bonding geometries (b, c) of methyl oxirane with a Si dimer.

between the radiation E-vector and the surface plane, and also on two different sample mountings with perpendicular Si dimer orientations. By curve fitting procedure, the components of Si 2*p* XPS are obtained.

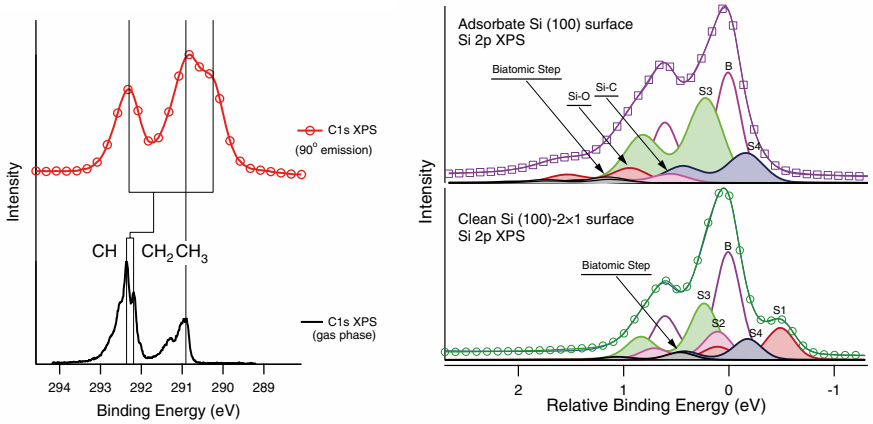

Figure 5.7: Left: Top curve: C 1*s* core-level photoemission spectrum of methyl oxirane on Si(100) 2×1 surface recorded at a photon energy of 350 eV and in normal emission. Bottom curve: gas-phase spectrum obtained at 340 eV photon energy [50, 51]. The spectral assignment for the free molecule in order of increasing binding energy is the following: C 1*s* emission from carbon of the CH_3 group, carbon of the CH_2 group, carbon of the CH group respectively. *Right*: Si 2p core-level spectra of clean and methyl oxirane-covered Si(100) 2×1 recorded at a photon energy of 150 eV and 45° emission. From top: deconvolution of the spectrum of the adsorbate-covered surface in components related to the atoms of the surface reconstruction with different environments, same for the clean surface[19], raw data.

By means of photoemission spectra, UPS and C 1*s*, Si 2*p* XPS, the ring opening of methyl oxirane, and cycloaddition with Si dimer can be confirmed.

Without the support of theory, present angular resolved NEXAFS hints to a "standing" geometry, (b) in Fig. 5.6.

5.2.2 Chemisorption of Ethylene Oxide

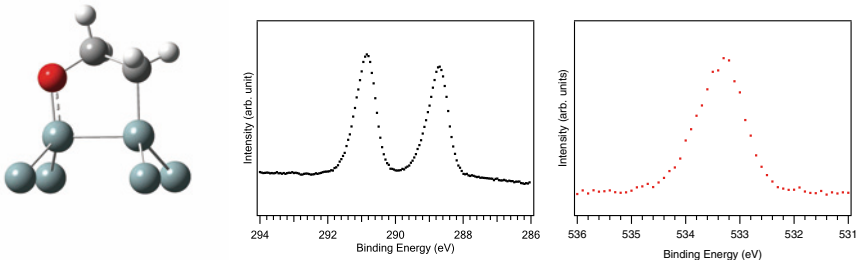

Figure 5.8: Left: Chemisorption geometry of ethylene oxide on Si (100) surface. *Center*: C 1s XPS and *Right*: O 1s XPS of ethylene oxide adsorbed on Si(100)-(2x1).

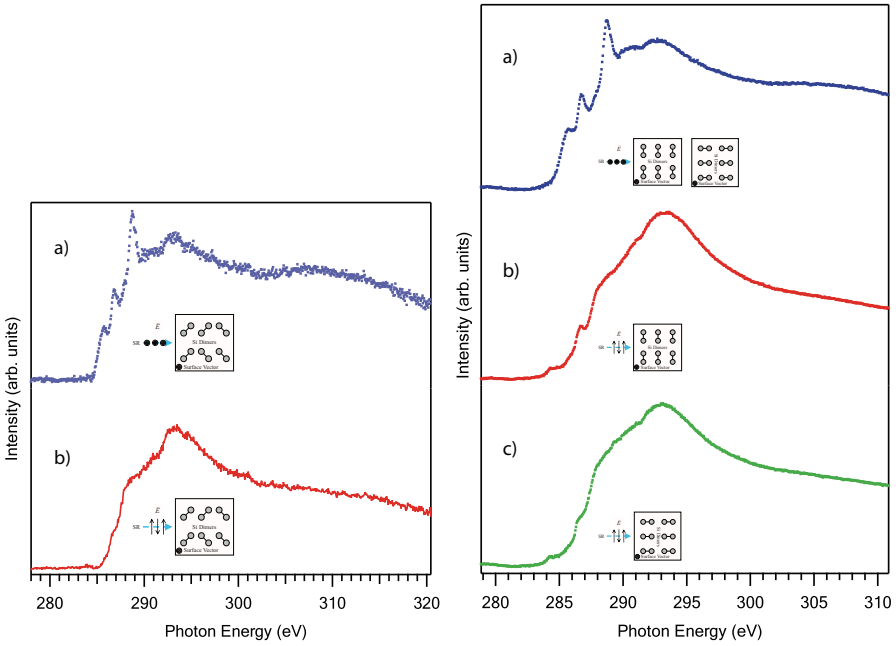

Figure 5.9: Left: Angular resolved NEXAFS of EO/Si (100)-(2×1) measured on a multi domain substrate. The insets illustrate the relative orientation of E-vector, Si dimer axis and substrate plane for the different spectra. *Right*: Angular resolved NEXAFS of EO/Si (100)-(2×1) measured on a single domain substrate. The insets illustrate the relative orientation of E-vector, Si dimer axis and substrate plane for the different spectra.

Ethylene oxide (EO) is the simplest epoxy molecule and as such the central building block of more complex epoxy molecules. In Paper **VII**, we present a

fundamental investigation of the adsorption of ethylene oxide on Si(100) with an combination of synchrotron based spectroscopies, such as core-level photo electron spectroscopy (XPS), valence band photo electron spectroscopy (UPS) and NEXAFS.

In Figure 5.8, the C 1*s* and O 1*s* XPS spectra indicate the bonding geometry of Figure 5.8 (a) and confirm the ring-opening reaction with CH_2-O bond breaking. From the Si 2*p* XPS spectrum, by a curve-fitting procedure, this structure was further confirmed by the existence of Si-O and Si-C components.

In Figure 5.9, the angular resolved NEXAFS spectra of single- and multi-domain samples are shown. In these spectra, three pronounced spectral features can be found in the geometry in which the radiation E-vector is normal to the sample surface. Excitation energies are around 285.7 eV, 286.8 eV, and 288.7 eV. They are assigned to excitations of C-Si bond, C-C bond and the combination of C-O and C-C bond. The strong and broad feature at excitation energy of 293.2 eV was assigned to the σ^*-type resonance in continuum.

5.2.3 Searching for Chiral Property of Adsorbates

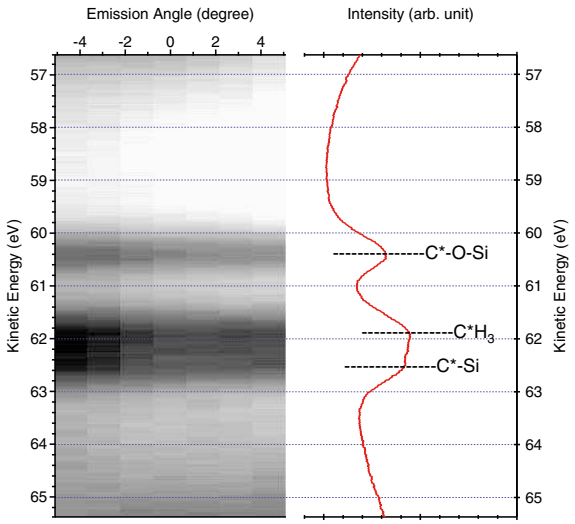

Figure 5.10: Left: Emission angle imaging of C 1*s* photoemission spectrum with a photon energy of 330 eV. *Right*: the integrated spectrum upon angles. The normal emission is set as 0˚ in the emission angle scale.

The chiralities of gas-phase and liquid-phase methyl oxirane have been intensively studied using optical rotation and VUV absorption circular dichroism method ([49] and references within). However, its significant chirality has not been experimentally discovered with core-level spectroscopy methods [52], especially for the surface adsorbed phase. In Paper **VII**, the chiral properties of chemisorbed enantiomers of methyl oxirane on Si (100) were tentatively

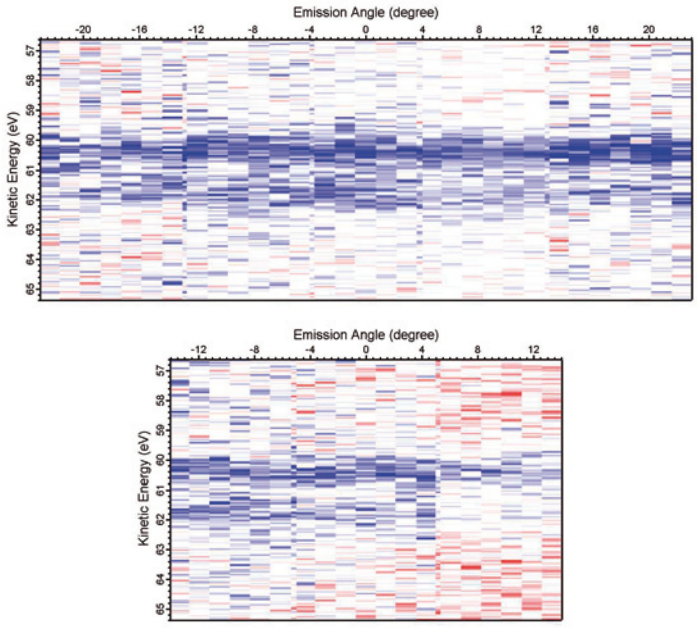

Figure 5.11: Up: Asymmetry factor for the S-enantiomer, calculated by subtracting the image obtained with right circularly polarized light from the image with left circular polarized light. *Down*: Asymmetry factor for the R-enantiomer, calculated by subtracting the image obtained with right circularly polarized light from the image with left circular polarized light. The blue color indicates positive value after the subtraction procedure and the red labels negative values

searched using the core-level (C 1*s*) photoemission CDAD (Circular Dichroism in Angular Distribution) method.

As shown in Figure 5.10, we have used the imaging method to obtain the energy dispersion of C 1s photoelectrons and the angular dispersion of photoionization yield simultaneously. Photoemission lines corresponding to the different C atoms in chemisorbed methyl oxirane molecule can be resolved. In Fig. 5.11, the asymmetry factors for the S-methyl oxirane and R-methyl oxirane are shown. The expecting sign changing effect was not observed. The same finding holds for the asymmetry factors for right circularly polarized light and left circularly polarized light. These observations which is negative for CDAD effect could be due to the coexistence of two different chemisorption species.

6. Conclusion and Outlook

In the present thesis, the basic concepts of synchrotron-radiation-related techniques and the theories needed to understand the experimental data are briefly described. In particular, two aspects of our research work are included. One is the experimental and theoretical study of electron spectroscopy of free molecules. The other one is the experimental study about surface adsorbate systems.

In the projects focusing on free molecules, a lot of effort has been paid to the understanding of molecular Auger electron spectra, including RAS and AES. We were able to perform a very detailed assignment of the Auger electron spectrum based on the *ab initio* calculation, vibrational structure simulation and experimental data. Another main achievement was the development of the new form of "one-step" model to include the PCI effect. In the foreseeing future, we are planing to complete this theory by applying it to different cases and knowing the possible effects. An expansion of this theory into the time-dependent domain to provide molecular nuclear dynamics information has been put in schedule. Further generalizations of the this formalism can lead to a molecular Auger emission theory which provides a full description of Auger processes including valence resonant Auger emission, Rydberg resonant Auger emission, shake down/up involved resonant Auger, photoelectron recapture phenomenon, and so on. This theory can be also further used in the surface chemistry process analysis by using Auger spectroscopy technique, and being dedicated to commercial purposes.

In the studying of surface-adsorbate systems, the presented results provide preliminary understandings of the chemisorption of epoxy molecules on Si (100) surface. More interesting topics are about another two epoxy molecules, cis-dimethyl oxirane and trans-dimethyl oxirane. The experimental data for these systems including core level and valence photoemission spectra and NEXAFS spectra were already obtained. NEXAFS has been proven to be a powerful tool to investigate the adsorbate geometries. To extract the angular information of NEXAFS, we have developed a new data treating method and a software for visualizing molecular coordinates and calculating angular resolved NEXAFS spectrum using the *ab initio* results of Gaussian 03. In near future, combining with the *ab initio* TD-DFT NEXAFS simulation results, we will systematically publish the studies and understandings of this group of chemicals. Apparently, these techniques can be generally applied to the study of other surface-adsorbate systems and free molecules. In recent years, RAS

(Resonant Auger Spectroscopy) technique has been developed to study the molecular core-hole nuclear and electronic dynamics and adsorbate-surface interactions. It strongly demands the understanding of core-excited state electronic structures and potential curves. With our method, this kind of information can be efficiently obtained.

Acknowledgments

Firstly, I would like to give my appreciations to my supervisors - Maria Novella Piancastelli, Svante Svensson and Denis Céolin - for the support and encouragement. Maria Novella Piancastelli granted me the opportunity to start my physical research work in Uppsala as a Ph. D. student, and led me into the scientific study fields using synchrotron radiation related techniques. Svante Svensson gave me a lot of suggestions on how research work should be performed and told us about the Swedish culture. Denis Céolin has taught me about the instruments on the beamline and showed me many interesting topics, like how to design a TOF. Reinhold F. Fink is the "supervisor" for my theory work. I would give my gratitude to him for his excellent teaching and great patience. He gave me the interest and confidence to go deeply into the theory.

Oksana Travnikova has been working together with me on our projects. We shared the offices and ideas. Thanks to her and good luck to her dissertation.

MAX-lab is almost my second home. Each time there for experiment, I have obtained great helps from the staff, especially, Franz Hennies and Maxim Tchaplyguine. Without their kindness and hard work, I can not imagine we could have enjoyed smooth experiments.

My first surface experiment class was given by Alexander Föhlisch, Mitsuru Nagasono and Franz. I will never forget that interesting event, thanks to them.

Thanks are also to Karsten Horn, Thorsten Kampen, Talia Deniozou and Thomas Braun for their kind supports in BESSY II. Surface CD experiment is never a easy thing.

In Japan, the synchrotron facility and beautiful old town are impressive, but the most unforgettable is the friends there, Professor Kiyoshi Ueda, Professor Hiroshi Tanaka, Georg Prümper, Yusuke Tamenori, Hironobu Fukuzawa, Takahiro Tanaka, James Harries and XiaoJing Liu.

I have been to the wonderful town of Bergen for several times. Professors Leif Sæthre and Knut Børve were always warm hosts. Thanks are also to Abusamha Mahmound for his kindness.

I would also say thanks to Gunnar Öhrwall, Olle Björneholm, Torbjörn Rander and Andreas Lindblad for the help they have granted. My gratitude are to all colleagues and people whom I have been working with.

Finally, thanks to my parents, all of your supports are the power keeping me going forward. I love you.

"You know? Making pizza is a little bit easier than dealing with Si (100) surface and programming with Igor is real fun."
Zhuo Bao

Bibliography

[1] David Attwood.
Soft X-Rays and Extreme Ultraviolet Radiation. Cambridge University Press, 1999. http://www.coe.berkeley.edu/AST/sxreuv/.

[2] Andrea Damasceli, Zahid Hussain, and Zhi-Xun Shen. *Rev. Mod. Phys.*, 75:473, 2003.

[3] SPECS GmbH. Technical note: Application of the phoibos.

[4] M. Bässler, A. Ausmees, M. Jurvansuu, R. Feifel, J. O. Forsell, P. de Tarso Fonseca, A. Kivimäki, S. Sundin, S. L. Sorensen, R. Nyholm, O. Björneholm, S. Aksela, and S. Svensson. *Nucl. Instrum. Methods A*, 469:382, 2001.

[5] R. Nyholm, S. Svensson, J. Nordgren, and A. Foldström. *Nucl. Instrum. Methods A*, 246:267, 1986.

[6] R. Denecke, P. Väterlein, M. Bässler, N. Wassdahl, S. Butorin, A. Nilsson, J. E. Rubensson, J. Nordgren, N. Mårtensson, and R. Nyholm. *J. Electr. Spectr. Rel. Phen.*, 101-103:971, 1999.

[7] K. J. S. Sawhney, F. Senf, M. Scheer, F. Schäfers, J. Bahrdt, A. Gaupp, and W. Gudat. *Nucl. Instr. Methods A*, 390:395, 1997.

[8] M. R. Weiss, R. Follath, K.J.S. Sawhney, F. Senf, J. Bahrdt, W. Frentrup, A. Gaupp, S. Sasaki, M. Scheer, H.-C. Mertins, D. Abramsohn, F. Schäfers, W. Kuch, and W. Mahler. *Nucl. Instr. Methods A*, 467-468:449, 2001.

[9] The ue56 undulators at bessy
. http://www.bessy.de/cms.php?idcatart=539.

[10] Johannes Bahrdt. APPLE II Undulators at BESSY, 2004.
http://hikwww1.fzk.de/anka/04-Bahrdt.pdf.

[11] H. Ohashi, E. Ishiguro, Y. Tamenori, H. Kishimoto, M. Tanaka, M. Irie, T. Tanaka, and T. Ishikawa. *Nucl. Instr. Methods A*, 486-487:529, 2001.

[12] T. Tanaka and H. Kitamura. *J. Synchrotron Radiat.*, 3:47, 1996.

[13] International Union of Crystallography 2000
. Principle of the figure-8 undulator design, 2000.
http://www.fr.iucr.org/s/issues/2000/03/00/hi0088/hi0088fig7.html.

[14] T. Tanaka, T. Hara, M. Oura, H. Ohashi, H. Kimura, S. Goto, Y. Suzuki, and H. Kitamura. *Rev. Sci. Instru.*, 70:4153, 1999.

[15] Stefan Franzen. Molecular Spectroscopy Lecture Notes, 1999.
http://chemdept.chem.ncsu.edu/ franzen/CH795Z/lecture/lecture.html.

[16] D. T. Colbert and W. H. Miller. *J. Chem. Phys.*, 96:1982, 1992.

[17] F. Kaspar, W. Domcke, and L. S. Cederbaum. *Chem. Phys. Lett.*, 44:133, 1977.

[18] M. N. Piancastelli, M. Neeb, A. Kivimäki, B. Kempgens, H. M. Köppe, K. Maier, A. M. Bradshaw, and R. F. Fink. *J. Phys. B*, 30:5677, 1997.

[19] M N Piancastelli, R F Fink, R Feifel, M Bässler, S L Sorensen, C Miron, H Wang, I Hjelte, O Björneholm, A Ausmees, S Svensson, P Sałek, F Kh Gel'mukhanov, and H Ågren. *J. Phys. B*, 33(9):1819–1826, 2000.

[20] S. L. Sorensen, R. Fink, R. Feifel, M. N. Piancastelli, M. Bässler, C. Miron, H. Wang, I. Hjelte, O. Björneholm, and S. Svensson. *Phys. Rev. A*, 64:012719, 2001.

[21] F. K. Gel'mukhanov, L. N. Mazalov, and A. V. Kondratenko. *Chem. Phys. Lett.*, 46:133, 1977.

[22] F. Gel'mukhanov and H. Ågren. *Phys. Reports*, 312:87, 1999.

[23] T. Åberg. *Phys. Scr.*, 21:495, 1980.

[24] J. J. Pireaux, S. Svensson, E. Basilie, P.-Å Malmqvist, U. Gelius, R. Caudano, and K. Siegbahn. *Phys. Rev. A*, 14(6):2133, 1976.

[25] J. J. Pireaux and R. Caudano. *Phys. Rev. B*, 15(4):2242, 1977.

[26] Kai siegbahn. *Science*, 217(9):111, 1982.

[27] http://spot.colorado.edu/ dessau/laserarpes.shtml.

[28] K. Siegbahn, C. Nordling, G. Johansson, J. Hedman, P. F. Heden, K. Hamrin, U. Gelius, T. Bergmark, L. O. Werme, R. Manne, and Y. Baer. *ESCA applied to free molecules*. North-Holland, Amsterdam, 1969.

[29] J. Adachi, N. Kosugi, and A. Yagishita. *J. Phys. B.*, 38:R127, 2005.

[30] Joachim Stöhr. *NEXAFS spectroscopy*. Springer-Verlag, June 1996. www-ssrl.slac.stanford.edu/stohr/nexafs.htm.

[31] P. Hohenberg and W. Kohn. *Phys. Rev.*, 136:B864, 1964.

[32] W. Kohn and L. J. Sham. *Phys. Rev.*, 140:A1133, 1965.

[33] G. E. Scuseria R. E. Stratmann and M. J. Frisch. *J. Chem. Phys.*, 109:8218, 1998.

[34] R. Bauernschmitt and R. Ahlrichs. *Chem. Phys. Lett.*, 256:454, 1996.

[35] K. C. Casida M. E. Casida, C. Jamorski and D. R. Salahub. *J. Chem. Phys.*, 108:4439, 1998.

[36] T. Åberg and G. Howat. Corpuscles and radiation in matter i. In S. Flugge and W. Mehlhorn, editors, *Encyclopedia of Physics*, volume 31, page 469. Springer, Berlin, 1982.

[37] R. X. Carroll, S. E. Anderson, L. Ungier, and T. D. Thomas. *Phys. Rev. Lett.*, 58:867, 1987.

[38] N. Correia, A. Flores-Riveros, H. Ågren, K. Helenelund, L. Asplund, and U. Gelius. *J. Chem. Phys.*, 83:2035, 1985.

[39] M. Neeb, J. E. Rubensson, M. Biermann, and W. Eberhardt. *J. Electron Spectrosc. Relat. Phenom.*, 67:261, 1994.

[40] M. Larsson, P. Baltzer, S. Svensson, B. Wannberg, and L. Karlsson. *J. Phys. B*, 23:1175, 1990.

[41] R. F. Fink. *J. Electron Spectrosc. Relat. Phenom.*, 76:295, 1995.

[42] R. Püttner, Y. F. Hu, G. M. Bancroft, H. Aksela, E. N ommiste, J. Karvonen, A. Kivimäki, and S. Aksela. *phys. rev. A*, 59:4438, 1999.

[43] R. Püttner, X.-J. Liu, H. Fukuzawa, T. Tanaka, M. Hoshino, H. Tanaka, J. Harries, Y. Tamenori, V. Carravetta, and K. Ueda. *Chem. Phys. Lett.*, 445:6¨C11, 2007.

[44] R. Püttner, I. Dominguez, T. J. Morgan, C. Cisneros, R. F. Fink, E. Rotenberg, T. Warwick, M. Domke, G. Kaindl, and A. S. Schlachter. *Phys. Rev. A*, 59:3415, 1999.

[45] T. Åberg. *Physica Scripta*, T41:71, 1992.

[46] S. Sundin, A. Ausmees, O. Björneholm, S. L. Sorensen, M. Wiklund, A. Kikas, and S. Svensson. *Phys. Rev. A*, 58(3):2037, 1998.

[47] H. M. Köppe, A. L. D. Kilcoyne, J. Feldhaus, and A. M. Bradshaw. *J. Electron. Spectrosc. Relat. Phenom.*, 75:97, 1995.

[48] J. Autschbach, T. Ziegler, S. J. A. van Gisbergen, and E. J. Baerends. *J. Chem. Phys*, 116:6930, 2002.

[49] M. Carnell, S. D. Peyerimhoff, A. Breest, K. H. Göderz, P. Ochmann, and J. Hormes. *Chem. Phys. Lett.*, 180:477, 1991.

[50] M. N. Piancastelli, T. Lischke, G. Prümper, X. J. Liu, H. Fukuzawa, M. Hoshino, T. Tanaka, H. Tanaka, J. Harries, Y. Tamenori, Z. Bao, O. Travnikova, D. Céolin, and K. Ueda. *J. Electron Spectrosc. Relat. Phenom.*, 156-158:259, 2007.

[51] Z. Bao, O. Travnikova, D. Céolin, and M. N. Piancastelli. *MAX-lab Report*, page 170, 2004.

[52] G. Prümper, T. Lischke, H. Fukuzawa, A. Reinköster, and K Ueda. *J. Phys. B: At. Mol. Opt. Phys.*, 40:3425–3434, 2007.

Part II:
Papers I-VII

Acta Universitatis Upsaliensis

Digital Comprehensive Summaries of Uppsala Dissertations from the Faculty of Science and Technology 420

Editor: The Dean of the Faculty of Science and Technology

A doctoral dissertation from the Faculty of Science and Technology, Uppsala University, is usually a summary of a number of papers. A few copies of the complete dissertation are kept at major Swedish research libraries, while the summary alone is distributed internationally through the series Digital Comprehensive Summaries of Uppsala Dissertations from the Faculty of Science and Technology. (Prior to January, 2005, the series was published under the title "Comprehensive Summaries of Uppsala Dissertations from the Faculty of Science and Technology".)

Distribution: publications.uu.se
urn:nbn:se:uu:diva-8610

ACTA
UNIVERSITATIS
UPSALIENSIS
UPPSALA
2008